The Astrophysical Journal, 906:90 (17pp), 2021 January 10 https://doi.org/10.3847/1538-4357/abc9c7

X-Ray Redshifts for Obscured AGN: A Case Study in the J1030 Deep Field

Alessandro Peca[1,2,3], Cristian Vignali[2,3], Roberto Gilli[2], Marco Mignoli[2], Riccardo Nanni[2,3,4], Stefano Marchesi[2,5], Micol Bolzonella[2], Marcella Brusa[2,3], Nico Cappelluti[1], Andrea Comastri[2], Giorgio Lanzuisi[2], and Fabio Vito[6]
[1] Department of Physics, University of Miami, Coral Gables, FL 33124, USA; alessandro.peca@miami.edu
[2] INAF—Osservatorio di Astrofisica e Scienza dello Spazio di Bologna, via Gobetti 93/3, 40129 Bologna, Italy
[3] Dipartimento di Fisica e Astronomia, Università degli Studi di Bologna, via Gobetti 93/2, 40129 Bologna, Italy
[4] Department of Physics, University of California, Santa Barbara, CA 93106-9530, USA
[5] Department of Physics and Astronomy, Clemson University, Kinard Lab of Physics, Clemson, SC 29634, USA
[6] Scuola Normale Superiore, Piazza dei Cavalieri 9, Pisa, Italy
Received 2020 June 18; revised 2020 November 4; accepted 2020 November 9; published 2021 January 12

Abstract

We present a procedure to constrain the redshifts of obscured ($N_H > 10^{22}$ cm^{-2}) active galactic nuclei (AGN) based on low count statistics X-ray spectra, which can be adopted when photometric and/or spectroscopic redshifts are unavailable or difficult to obtain. We selected a sample of 54 obscured AGN candidates on the basis of their X-ray hardness ratio, HR > -0.1, in the Chandra deep field (∼479 ks, 335 arcmin^2) around the $z = 6.3$ QSO SDSS J1030 +0524. The sample has a median value of ≈80 net counts in the 0.5–7 keV energy band. We estimate reliable X-ray redshift solutions taking advantage of the main features in obscured AGN spectra, like the Fe 6.4 keV Kα emission line, the 7.1 keV Fe absorption edge, and the photoelectric absorption cutoff. The significance of such features is investigated through spectral simulations, and the derived X-ray redshift solutions are then compared with photometric redshifts. Both photometric and X-ray redshifts are derived for 33 sources. When multiple solutions are derived by any method, we find that combining the redshift solutions of the two techniques improves the rms by a factor of 2. Using our redshift estimates ($0.1 \lesssim z \lesssim 4$), we derived absorbing column densities in the range $\sim 10^{22}$–10^{24} cm^{-2} and absorption-corrected, 2–10 keV rest-frame luminosities between $\sim 10^{42}$ and 10^{45} erg s^{-1}, with median values of $N_H = 1.7 \times 10^{23}$ cm^{-2} and $L_{2-10\,\mathrm{keV}} = 8.3 \times 10^{43}$ erg s^{-1}, respectively. Our results suggest that the adopted procedure can be applied to current and future X-ray surveys for sources detected only in X-rays or that have uncertain photometric or single-line spectroscopic redshifts.

Unified Astronomy Thesaurus concepts: Active galactic nuclei (16); X-ray active galactic nuclei (2035); Spectral energy distribution (2129); X-ray surveys (1824); Redshift surveys (1378); AGN host galaxies (2017)

1. Introduction

Active galactic nuclei (AGN) are the observed manifestation of gas accretion onto supermassive black holes (SMBHs). The energy produced in this process can be observed from radio frequencies to X-rays and can dominate the host galaxy emission. However, the AGN radiation can be extinguished by gas and dust along our line of sight, making the detection of the AGN processes very challenging. Following the unified model for AGN (Antonucci 1993; Urry & Padovani 1995), the presence of parsec-scale circumnuclear material distributed in a toroidal shape may partially or completely hide the nuclear activity. In this case, the stellar emission from the host galaxy significantly dilutes the radiation produced by SMBH accretion, especially in the optical/near-infrared (ONIR) bands (e.g., Hickox & Alexander 2018), hiding the AGN from our view. In this scenario, the high-energy X-ray photons can penetrate through high column densities, making the detection of the obscured AGN ($N_H > 10^{22}$ cm^{-2}) possible. In addition, the X-ray radiation does not suffer from significant contamination because of the very low contribution from stellar processes at typical AGN luminosity regimes ($L_X > 10^{42}$ erg s^{-1}; e.g., Padovani et al. 2017). Therefore, X-ray surveys are the best tool for revealing and characterizing the large population of obscured and faint AGN, which is predicted by X-ray background models (e.g., Comastri et al. 1995; Treister & Urry 2006; Gilli et al. 2007; Ananna et al. 2019) but the most challenging to detect. In particular, to reveal mildly and heavily obscured ($N_H > 10^{23}$ cm^{-2}) objects, very deep X-ray surveys (see Brandt & Alexander 2015 for a review) are fundamental. It is worth mentioning that the far-infrared/radio band is also effective in selecting obscured AGN, but due to the relatively modest sensitivities of the current facilities, its potential is not yet fully exploited (e.g., Hickox & Alexander 2018).

Obscured AGN are the most abundant class of objects revealed in deep X-ray surveys (e.g., Ueda et al. 2003; Aird et al. 2015; Buchner et al. 2015), and measuring their redshift is notoriously complicated but at the same time crucial to understand their demography and their role in the AGN cosmological evolution. The ONIR spectroscopy is commonly used to provide the best redshift estimates because of the uniquely identifiable emission and absorption features at these wavelengths. However, it is costly in terms of observing time and suffers from extinction, making it not always feasible for faint sources. Photometry is then commonly used to build the spectral energy distribution (SED) of such targets, providing a photometric redshift estimate (z_{phot}) whose accuracy depends on the data quality, the availability of suitable SED templates for the fitted objects, and the number of available filters. Since for obscured AGN, the radiation emitted by nuclear accretion is expected to be heavily suppressed in the ONIR bands, the photometric points are mostly representative of the stellar emission. Therefore, simple galaxy templates can be used for the SED fitting without the need of introducing hybrid (AGN + stellar) templates, which would produce degenerate redshift solutions (Salvato et al. 2009). However, especially for sources detected in the ONIR wave bands with a low signal-to-noise ratio and in a limited number of filters, photometric redshifts may be uncertain and not reliable (e.g., Salvato et al. 2019).

For these reasons, redshift estimates based on X-ray features in obscured AGN have been attempted (e.g., Maccacaro et al. 2004; Braito et al. 2005; Civano et al. 2005; Iwasawa et al. 2012; Vignali et al. 2015). This relatively new and promising technique relies on the main X-ray spectral features, like the Fe Kα emission line and absorption edge, which become particularly prominent in heavily obscured objects (e.g., Ghisellini et al. 1994; Ikeda et al. 2009), allowing their identification and, consequently, the redshift estimate. The X-ray redshifts (z_X) were recently measured for hundreds of AGN in different surveys (e.g., Simmonds et al. 2018; Iwasawa et al. 2020) and also for galaxy clusters (e.g., based on the K-shell Fe line complex at 6.7–6.9 keV; Yu et al. 2011), with different approaches, selection criteria, and photon statistics. We explore here a method to constrain the redshifts of obscured AGN using low count statistics X-ray spectra, down to ~30 counts. The X-ray redshift solutions are derived from the combination of spectral analysis and ad hoc spectral simulations, where the instrument response, a proper background sampling, and their off-axis dependencies are taken into account. The obtained X-ray redshift solutions are also compared with photometric redshifts, derived from SED fitting. We show that the derived redshift quality is sufficient to calculate the main physical properties of obscured AGN, such as X-ray luminosity and absorption column density. The proposed method can be applied to current X-ray surveys performed with Chandra and XMM-Newton, the forthcoming eROSITA All-Sky Survey (eRASS), and future X-ray missions.

The paper is organized as follows. In Section 2, we present the multiband data used in this work. In Section 3, we describe the X-ray spectral analysis and the simulations used to estimate the X-ray redshifts. In Section 4, we describe the SED fitting procedure. The main results are presented in Section 5, where we also show the derived AGN physical properties of our sample. Our results are discussed in Section 6 and summarized in Section 7. Throughout this paper, we assume a LCDM cosmology with the fiducial parameters $H_0 = 70$ km s^{-1} Mpc^{-1}, $\Omega_M = 0.3$, and $\Omega_\Lambda = 0.7$, close to the Planck 2015 results (Planck Collaboration et al. 2016). All magnitudes are in the AB system (Oke 1974), and the errors are reported at the 1σ confidence level if not specified otherwise.

2. Data Set and Sample Selection

Our study uses data from the deep X-ray survey field centered on the $z = 6.31$ quasar SDSS J1030+0524 (hereafter the J1030 field; Nanni et al. 2018). This area was extensively covered by a large number of deep and wide multiband observations (details on the J1030 website[7]). A summary of the X-ray and optical/infrared data sets used in this work is reported below.

2.1. Chandra Observations

The J1030 field was observed by Chandra/ACIS-I with 10 different pointings between 2017 January and May, for a total exposure time of ~479 ks and a field of view of 335 arcmin^2. This set of observations makes the J1030 field one of the deepest extragalactic X-ray surveys performed so far, allowing us to investigate the obscured AGN population up to high redshift and down to limiting fluxes of ~3, 0.6, 2×10^{-16} erg s^{-1} cm^{-2} in the 0.5–7 (full), 0.5–2 (soft), and 2–7 (hard) keV bands, respectively. Different from the other Chandra deep/moderately deep fields (e.g., CDF-S, Giacconi et al. 2001; Luo et al. 2017; COSMOS-Legacy, Civano et al. 2012; Marchesi et al. 2016a), the J1030 field has not yet benefited from decades of spectroscopic follow-ups. The details of the observations and data reduction are given in Section 2 of Nanni et al. (2018). The source catalog (Nanni et al. 2020, hereafter N20) has been generated using *wavdetect* (Freeman et al. 2002) for the source detection and CIAO ACIS EXTRACT (Broos et al. 2010) for the source photometry and significance assessment. The final catalog contains 256 X-ray sources. These have then been matched with the available optical/infrared catalogs using a likelihood ratio technique (e.g., Ciliegi et al. 2003; Brusa et al. 2007; Luo et al. 2010); 252 of them have a counterpart in these wave bands (see N20 for further details).

2.2. Optical/Infrared Imaging

In 2012, the J1030 field was observed with the Large Binocular Telescope (LBT) using the Large Binocular Camera (LBC) to obtain imaging of a $23' \times 25'$ area in the *r*, *i*, and *z* bands (Morselli et al. 2014) down to limiting AB magnitudes of 27.5, 25.5, and 25.2, respectively. In 2015, we performed a $24' \times 24'$ observation in the near-infrared *Y* and *J* bands (Balmaverde et al. 2017) at the Canada–France–Hawaii Telescope (CFHT) using WIRCam, with limiting AB magnitudes of 23.8 and 23.75, respectively.

The field is one of the four fields included in the Multi-wavelength Survey by Yale-Chile (MUSYC). Three MUSYC catalogs are available for J1030: the BVR catalog, obtained by selecting sources in the BVR stacked image down to 26.3 AB magnitudes (Gawiser et al. 2006), and the *K*-wide (Blanc et al. 2008) and *K*-deep (Quadri et al. 2007) catalogs, performed selecting sources in the *K* band down to $K = 21$ and 23 AB, respectively. As shown in Figure 1, the MUSYC BVR and *K*-wide data cover a $30' \times 30'$ area, while the MUSYC *K*-deep covers a smaller $10' \times 10'$ area. Furthermore, the field has been observed by the Spitzer Infrared Array Camera (IRAC) in the mid-infrared (MIR) at 3.6 and 4.5 μm. In this work, we used the available catalogs and images in the IRSA[8] archive that reach a depth of 22–23 AB magnitudes. All of the optical/infrared data sets and filters used in this paper are discussed in Section 4.

2.3. Sample Selection

From the X-ray catalog, we selected a sample of 54 obscured AGN candidates on the basis of their hardness ratio (HR), defined as

$$\mathrm{HR} = \frac{H - S}{H + S}, \quad (1)$$

where *H* and *S* are the net count rates (i.e., background subtracted) in the hard and soft bands, respectively. Since the AGN X-ray emission is more absorbed at low energies, the HR value can be considered a good proxy of absorption for AGN with known redshift and simple (absorbed power-law) spectra (e.g., Mainieri et al. 2002).

However, the Chandra/ACIS-I photon collecting efficiency is rapidly decreasing in the soft band due to contamination (see the

[7] http://j1030-field.oas.inaf.it/

[8] https://irsa.ipac.caltech.edu/

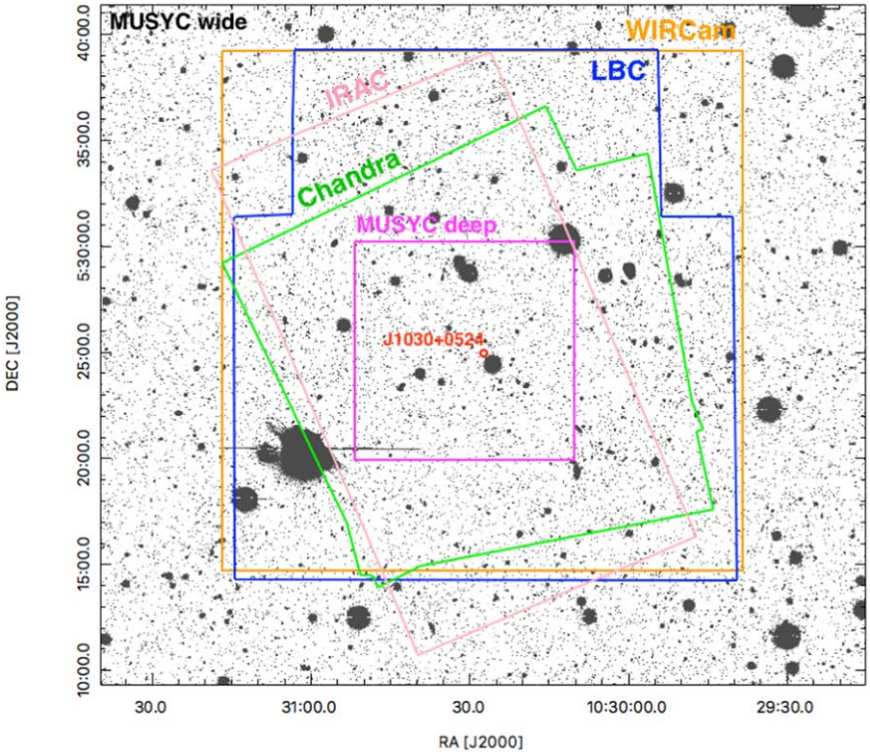

Figure 1. Multiwavelength coverage of the J1030 field used in this work: Chandra/ACIS-I (green), LBT/LBC (blue), CFHT/WIRCam (orange), MUSYC *K*-deep (magenta), and Spitzer/IRAC from the IRSA online archive (pink). The background image is the MUSYC BVR stacked image, while the $z = 6.31$ QSO SDSS J1030 +0524 is highlighted in red.

Chandra Proposers' Observatory Guide[9]), making the HR a time-dependent quantity. This decrease has accelerated over the last few years, thus allowing only a qualitative comparison with previous works (e.g., Tozzi et al. 2001; Szokoly et al. 2004), as explained in Appendix A. Therefore, we performed X-ray spectral simulations based on the J1030 Chandra observations to reproduce the expected trends for our sample. The simulations were performed through XSPEC[10] v.12.9.1 (Arnaud 1996), assuming an absorbed power-law model at different redshifts (`zphabs×powerlaw`). The mean Galactic absorption at the J1030 field position, $N_H = 2.6 \times 10^{20}\,\mathrm{cm}^{-2}$ (Kalberla et al. 2005), was also considered (`phabs`). In Figure 2, we show the HR values for typical AGN column densities ($10^{21}\,\mathrm{cm}^{-2} \leqslant N_H \leqslant 10^{24}\,\mathrm{cm}^{-2}$) as a function of redshift and with a canonical photon index $\Gamma = 1.9 \pm 0.2$ (e.g., Nandra & Pounds 1994; Piconcelli et al. 2005; Lanzuisi et al. 2013a). It is worth mentioning that these curves are computed for simulated spectra with thousands of counts to reproduce the expected HR trends (e.g., Szokoly et al. 2004; Elvis et al. 2012). Based on our simulations, we chose a threshold of HR > -0.1 (black horizontal line) to select obscured AGN. In fact, considering $\Gamma = 1.9$, this threshold allows the selection of obscured objects with $N_H \geqslant 10^{22}\,\mathrm{cm}^{-2}$ up to $z \approx 0.5$, $N_H \geqslant 10^{23}\,\mathrm{cm}^{-2}$ up to $z \approx 2.5$, and Compton-thick AGN ($N_H \gtrsim 10^{24}\,\mathrm{cm}^{-2}$) at all redshifts. If we instead consider a flatter ($\Gamma = 1.7$) or steeper ($\Gamma = 2.1$) power law, we obtain more positive or negative HR, respectively, but, in both cases, the chosen HR > -0.1 threshold avoids the selection of unobscured sources at any redshift. Due to the limited photon statistics in our sample, we assumed a basic model to compute

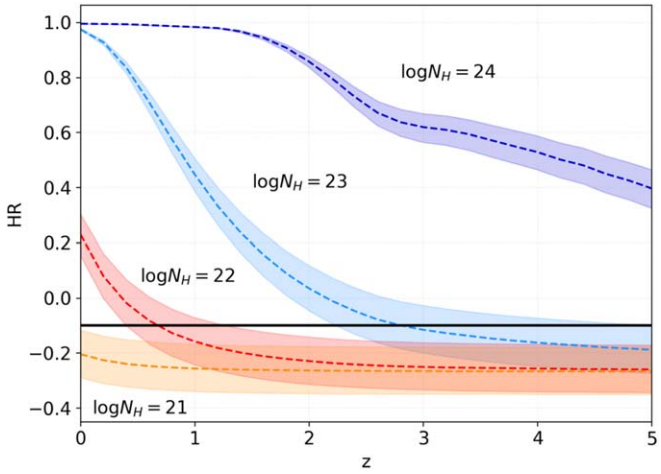

Figure 2. The HR as a function of redshift for different absorption column densities in color code. The shaded areas indicate HR values derived with fixed $\Gamma = 1.7$ (top curves) and $\Gamma = 2.1$ (bottom curves), while the dotted lines represent models with $\Gamma = 1.9$. We used the response matrices at the aimpoint of the Chandra observations. The black horizontal line represents the chosen selection threshold HR $= -0.1$.

the different N_H curves shown in Figure 2. Despite this, if we consider more complex models, the chosen HR threshold remains valid (see Appendix B). In addition to the HR criterion, we selected sources detected in N20 with at least 50 net counts in the 0.5–7 keV band to allow an effective search for X-ray spectral features, such as the 6.4 keV Fe Kα emission line and the 7.1 keV Fe absorption edge. For sources not detected in one or two bands, N20 reported the 3σ net counts upper limits. Because we were looking for relatively hard objects, we considered an HR $= 1$ for sources undetected in

[9] https://cxc.harvard.edu/proposer/POG/
[10] https://heasarc.gsfc.nasa.gov/xanadu/xspec/

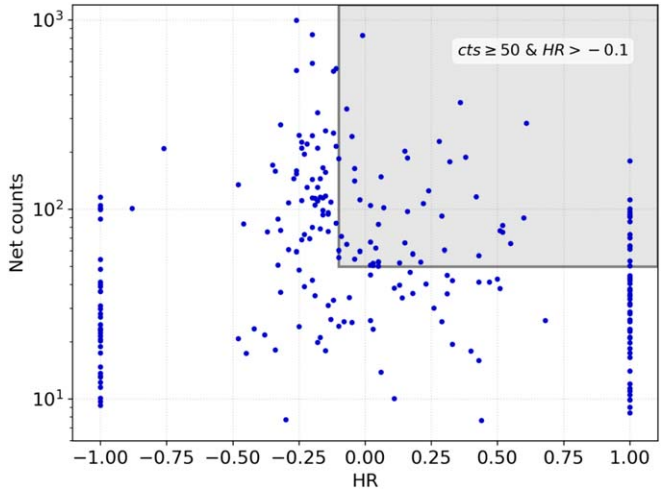

Figure 3. The HR vs. full-band net counts from the J1030 X-ray catalog. The gray top right corner shows the region with HR > -0.1 and net counts $\geqslant$50 used to select our sample of 54 obscured AGN candidates.

the soft band and HR $= -1$ for sources undetected in the hard band. We discarded 11 sources detected in the full band only. The final sample and adopted selection criteria are shown in Figure 3.

3. X-Ray Data Analysis

3.1. Spectral Analysis

The spectral extraction was made using the Chandra Interactive Analysis of Observations[11] (CIAO) v.4.9 software. The choice of the extraction regions was performed by taking into account the source position on the detector, since the point-spread function (PSF) broadens as the off-axis angle (θ) increases. As the extraction radius, we use the 90% encircled energy radius ($E = 1.49$ keV) at the source position, and, to increase the signal-to-noise ratio of the faintest sources, we manually chose ad hoc slightly smaller radii. The regions used to extract the background spectra were selected next to each source and, to ensure a good background sampling, with an area at least 10 times larger. We extracted a spectrum from each observation covering a given source and then combined these spectra using the CIAO tool COMBINE_SPECTRA. The source spectra were grouped to a minimum of one count per energy bin to avoid empty channels. We checked the presence of at least one background count in each source energy bin and then adopted the modified C-statistic for direct background subtraction (Cash 1979; Wachter et al. 1979) or W-statistic to estimate the best-fit model parameters. The spectral analysis was performed using XSPEC v.12.9.1 (Arnaud 1996).

Our sample of 54 objects has a median value of $\approx$80 net counts in the 0.5–7 keV energy range and median fluxes of 6.8, 1.0, 5.4 $\times$ 10^{-15} erg s^{-1} cm^{-2} in the full, soft, and hard bands, respectively. Given the low photon statistics, we adopted a simple model based on a power law, an intrinsic N_H at the source redshift z, and Galactic absorption at the source position (`phabs(zphabs×powerlaw)`). The photon index Γ was fixed to 1.9, as commonly observed in AGN (e.g., Nandra & Pounds 1994; Lanzuisi et al. 2013a). We left the intrinsic N_H, z, and power-law normalization free to vary. To investigate the presence of emission lines, we included a redshifted Gaussian feature at 6.4 keV rest frame (`zgauss`) with a redshift parameter anchored to the corresponding absorption component, a free normalization, and a fixed line width $\sigma = 10$ eV (e.g., Nanni et al. 2018), which takes into account only the narrow component produced far away from the central SMBH by the absorbing cold medium, since the broad, relativistic component produced in the accretion disk is expected to be obscured (e.g., Risaliti & Elvis 2004). Using a simple absorbed power law plus a Gaussian line may not be a detailed description of the X-ray spectrum. Nevertheless, the limited count statistics did not allow an investigation of more complex spectral shapes (e.g., Lanzuisi et al. 2013a; Iwasawa et al. 2020). This choice is also justified by a few tests on more complex models, showed in Appendix B.2. In case of heavy obscuration, the main AGN features, such as the Fe Kα 6.4 keV line and the 7.1 keV Fe edge, become more prominent (e.g., Iwasawa et al. 2012) and easily recognizable, as shown in Figure 4. Once one of these features was identified, a redshift solution from the X-ray spectrum (hereafter z_X) was derived by evaluating the redshift-likelihood profile, computed with the STEPPAR command. An example is reported in Figure 5. We considered to be reliable z_X those solutions where the difference in the C-statistic (ΔC) between the global minimum (primary solution, i.e., the best-fit redshift) and its nearby maximum is at least 2.71, corresponding to a fit improvement at the 90% confidence level (see, e.g., Tozzi et al. 2006 and Brightman et al. 2014, who validated this threshold through simulations). We also investigated local minima (secondary solutions) where the above ΔC criterion was satisfied, as for the case in Figure 5. Each selected z_X was then further investigated through simulations.

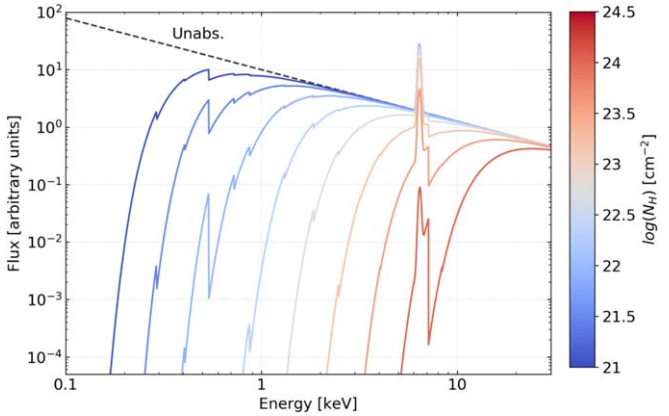

Figure 4. The X-ray AGN spectral model as a function of the absorption column density, N_H, in color code. The assumed model is a power law (`powerlaw`) with $\Gamma = 1.9$, a fixed Gaussian line at 6.4 keV rest frame with $\sigma = 10$ eV (`zgauss`), and an absorption component (`zphabs`). The plotted curves are for $z = 0$.

3.2. X-Ray Spectral Simulations

Estimating the goodness of an X-ray spectral fit is not trivial in the case of low count statistics. We therefore built two different sets of spectral simulations to test the derived X-ray redshift solutions. The first set of simulations aims at verifying the significance of the candidate emission lines (Section 3.2.1), and the second aims at constraining for which photon statistics, as a function of N_H, z, and θ, we expect to obtain robust redshifts from X-ray data alone (Section 3.2.2). All simulated spectra were obtained using the XSPEC FAKEIT command.

[11] http://cxc.harvard.edu/ciao/

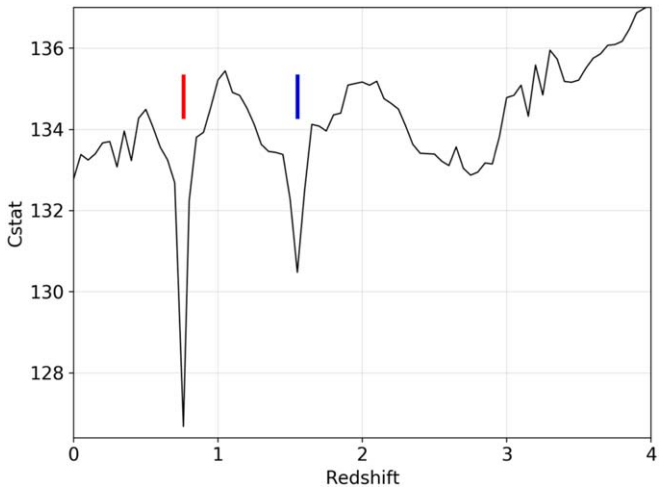

Figure 5. Redshift-likelihood profile in terms of the C-statistic for one source (XID 70) of the selected sample. In red and blue are the primary and secondary z_X solutions, respectively. The profile was computed through the STEPPAR command with a redshift step of $\Delta z = 0.05$.

3.2.1. Line Significance

The simulations reported in this paragraph refer to sources where the redshift estimate is driven by the iron Kα emission line. For each source in which the line was possibly detected, we established a significance criterion to deem a candidate emission line as reliable as follows (e.g., Lanzuisi et al. 2013b; Vignali et al. 2015). Because we do not know the redshift of the sources, we fitted the spectra using an absorbed power-law model (`phabs×powerlaw`; $\Gamma = 1.9$) with and without a Gaussian line (`gauss`; $\sigma = 10$ eV). For the former, the line energy was fixed to the observed value. The best-fit parameters from the model without the line were then used to simulate 1000 spectra with the same characteristics (response matrices,[12] exposure time, background and photon statistics) as the observed one. We fitted the simulated spectra using exactly the two models, fixing the continuum to the one derived from the model without the line and leaving the line energy free to vary, looking for all cases where

$$\Delta C_{\rm sim} \geqslant \Delta C_{\rm obs}, \quad (2)$$

where $\Delta C_{\rm obs}$ is the difference between the best-fit model with and without the possible line in the observed spectrum, while $\Delta C_{\rm sim}$ is the difference between the same models in each simulated spectrum. The frequency at which Equation (2) occurs corresponds to the probability P' that the detected line is just a statistical fluctuation. Then

$$P_{\rm sim} = (1 - P') \quad (3)$$

corresponds to the significance of the observed line. We considered an emission line reliable when $P_{\rm sim} \geqslant 90\%$.

Since calculating $P_{\rm sim}$ is time-consuming, we proceeded as follows. The F-test is a fast method to evaluate the model improvement due to an additive component, but in the case of a Gaussian line, it is considered inappropriate (Protassov et al. 2002). However, allowing the line normalization to also be negative,[13] it can be used as an indication of the model improvement. After extensive testing on our data set, we found that, to obtain a reliable line (i.e., with $P_{\rm sim} \geqslant 90\%$), an F-test probability ($P_{\rm Ft}$) $> 99\%$ is required. We then decided to use the F-test as prescreening. When the $P_{\rm Ft}$ threshold is reached, the significance ($P_{\rm sim}$) of the candidate lines is computed through the aforementioned simulations to provide a more solid evaluation. When a significant line has been found, it is used to derive an X-ray redshift solution, assuming that the detected line is the Fe Kα fluorescent emission line at 6.4 keV, which is the most probable emission line in the AGN X-ray spectrum (e.g., Fabian et al. 2000). Otherwise, the z_X determination is principally driven by the Fe 7.1 keV edge coupled with the photoelectric absorption cutoff.

3.2.2. Redshift Solutions as a Function of N_H, Net Counts, and Off-axis Angle

To verify the level of photon statistics allowing the redshifts to be derived from the X-ray analysis, we performed a second set of simulations. We simulated spectra not only with different AGN parameters but also using different responses and backgrounds, as these vary with the off-axis angle. This set of simulations aims to be global, i.e., reliable in every position of the observations, and it was used to further investigate the derived X-ray redshift solutions. To test the z_X driven by absorption features, we adopted an absorbed power-law model (`zphabs×powerlaw`) with a fixed intrinsic photon index $\Gamma = 1.9$, while for redshift solutions driven by the Fe Kα line, we also included a redshifted Gaussian line (`zgauss`) at 6.4 keV rest frame, with a width of $\sigma = 10$ eV. We set different line normalizations to obtain a canonical range of rest-frame equivalent widths, between 10 eV and 2 keV, as a function of N_H (e.g., Ghisellini et al. 1994; Lanzuisi et al. 2015). In both models, we added an additional absorption component (`phabs`) with a fixed value of $N_H = 2.6 \times 10^{20}$ cm^{-2}, corresponding to the mean Galactic absorption at the J1030 field position. To reproduce what is observed in deep X-ray surveys (e.g., Tozzi et al. 2006; Marchesi et al. 2016a), we simulated column densities from $N_H = 10^{21}$ to 10^{24} cm^{-2} with a logarithmic step of 0.5, redshifts up to 5 with a step of 0.5, and different power-law normalizations to obtain a number of full-band net counts in the range 10–1000. For each parameter combination, 500 spectra were simulated.

To simulate spectra that are as close as possible to those observed in the Chandra data, the response matrices of the real observation must be used. In general, the instrumental response drops as the off-axis angle increases, which therefore has to be taken into account. Assuming no azimuthal dependence of the instrument response, we extracted the ancillary response file (ARF) and the redistribution matrix file, for four relatively bright sources at different off-axis angles ($\theta \sim 0'$, $3\farcm2$, $5\farcm0$, and $9\farcm5$) in order to reproduce the decrease of the effective area as a function of θ (Figure 6). In addition, it is necessary to evaluate the background spectra to be associated with the simulated source spectra. Assuming that the background only varies with the off-axis angle and has no azimuthal dependence, we extracted background spectra using a circular region of $r = 2'$ centered at the aimpoint and annuli of width $1'$ at a distance of $3\farcm5$, $5\farcm5$, and $9\farcm5$ from the aimpoint. To get a suitable background, the sources present in such regions were excluded. We used the CIAO tool DMCOPY through the command EXCLUDE to remove X-ray sources identified by N20 in the J1030 field. The extracted background also needs to be rescaled by the source extraction area before being associated with it.

[12] Ancillary response file and redistribution matrix file.
[13] https://asd.gsfc.nasa.gov/XSPECwiki/statistical_methods_in_XSPEC

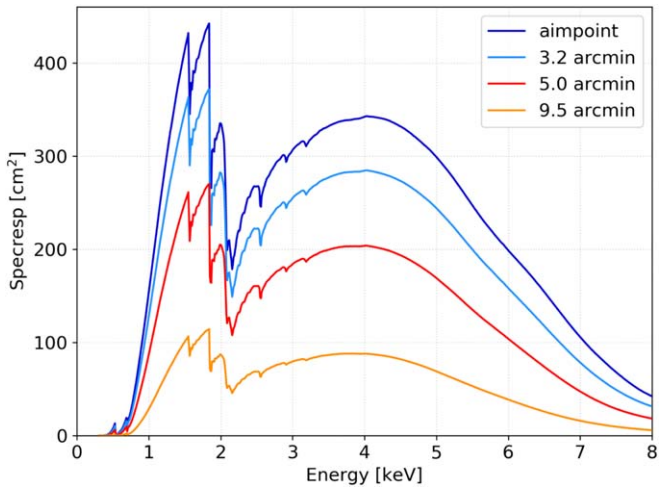

Figure 6. The ARFs selected for the simulations at different off-axis angles from the aimpoint. As discussed in the text, the instrument's response decreases as the off-axis angle increases.

Since the sources are simulated, they do not have a physical extraction region, so we rescaled the background to the width of the PSF (90% encircled energy radius at $E = 1.49$ keV) at specific off-axis angles.

For each parameter combination (N_H, z, net counts, and θ), 1000 spectra were simulated, for a total of 800,000. For each simulated spectrum, a fit was performed, and the best-fit redshift solution, z_X, was derived. We then computed the match percentage,

$$\text{match } \%\ (z, N_H, \text{counts}, \theta) = \frac{N(z_X \pm \Delta z)}{N(z_{\text{sim}})}, \tag{4}$$

that corresponds, for a specific range of redshift, N_H, number of net counts, and θ, to the number of simulated spectra in which z_X is consistent with the simulated redshift (z_{sim}) within a given tolerance Δz, normalized to the total number of simulated spectra. Because of the low count statistics, the X-ray redshift solutions are sometimes poorly constrained. To determine if the redshift solutions are reliable, we rejected solutions with $|\Delta z| > 0.15(1 + z_{\text{sim}})$, defined as outliers (this value has been found in previous works to be a reliable boundary for outliers; e.g., Hsu et al. 2014; Ananna et al. 2017; Luo et al. 2017; Simmonds et al. 2018). For a conservative approach, we discarded redshift solutions that are either upper or lower limits. We also checked the N_H values, rejecting solutions that are not consistent within the errors with the simulations, even if the redshift solutions are good (∼6%). An example of the simulations' performance is shown in Figure 7, where it is clear how column densities $\geqslant 10^{22}$ cm^{-2} are needed to obtain a reliable z_X for sources with a net count range as in our sample. Furthermore, the match percentage depends on redshift. If no emission lines are detected, the X-ray solutions are driven by the iron absorption edge coupled with the photoelectric cutoff, but, moving toward high redshift ($z > 3$–4), such an absorption complex ends up at $\lesssim$1.5 keV, where the effective area decreases dramatically. As a consequence, the match percentage decreases as the redshift increases. Besides showing how the main features of the X-ray spectrum become more prominent with increasing obscuration, and therefore more easily identifiable, the simulations

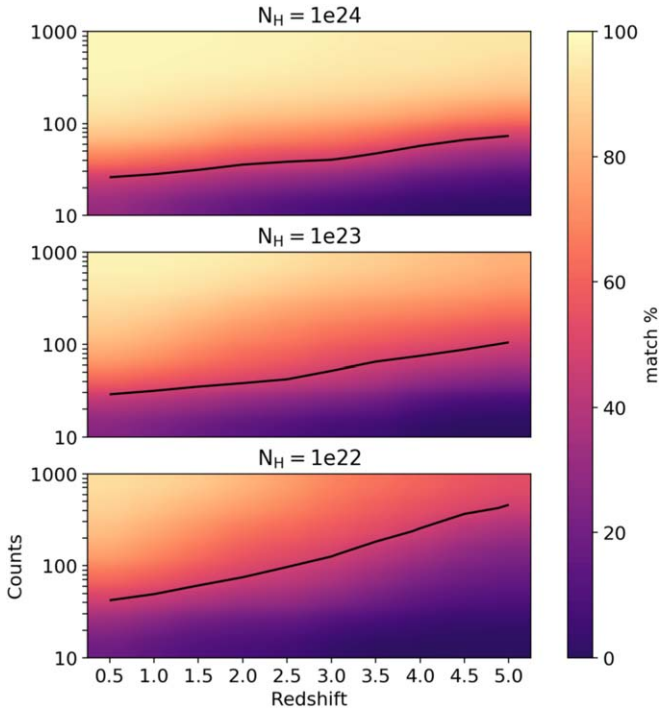

Figure 7. Simulation results for a source located within 2′ from the aimpoint, where the redshift solutions are derived using only absorption features. The three panels indicate different absorption values: $N_H = 10^{24}$, 10^{23}, and 10^{22} cm^{-2}, from top to bottom. Each panel shows the match percentage (Equation (4)) in color code, smoothed for graphical purposes, as a function of redshift and net counts. The black solid lines represent the 50% confidence curves, above which z_X are considered reliable solutions. The simulation has a resolution of 20 net counts.

give us an indication of the probability of deriving a correct redshift or not. We set a match percentage threshold of at least 50% to accept z_X solutions driven by absorption features. In this regard, we found reliable solutions down to a regime of ∼30 net counts for redshift $\lesssim$2.5 and $N_H > 10^{23}$ cm^{-2}. For z_X solutions derived from the Fe Kα line instead, we considered this 50% threshold as an additional check, since it confirms the results obtained from Section 3.2.1. In our sample, where it was possible to derive an X-ray redshift solution (38 sources), the chosen threshold returns a mean match percentage of ∼70%. The full procedure adopted for the z_X estimate is summarized in Figure 8.

4. Photometric Data Analysis

4.1. Data Modeling

We used the available data sets in the optical and infrared bands to calculate photometric redshifts (hereafter z_{phot}) through an SED fitting procedure and test the X-ray redshift solutions. Photometric redshifts were obtained through the *hyperz* code (Bolzonella et al. 2000) using a variety of galaxy templates, detailed below, and a Calzetti et al. (2000) reddening law. The code finds the best-fit template through a standard χ^2 minimization procedure, comparing template spectra to the observed SEDs as

$$\chi^2(z) = \sum_{i=1}^{N_{\text{filters}}} \left[\frac{F_{\text{obs},i} - b \times F_{\text{temp},i}(z)}{\sigma_i} \right]^2, \tag{5}$$

where $F_{\text{obs},i}$ and $F_{\text{temp},i}$ are the observed and template fluxes, σ_i is the observed flux uncertainty, and b is a normalization

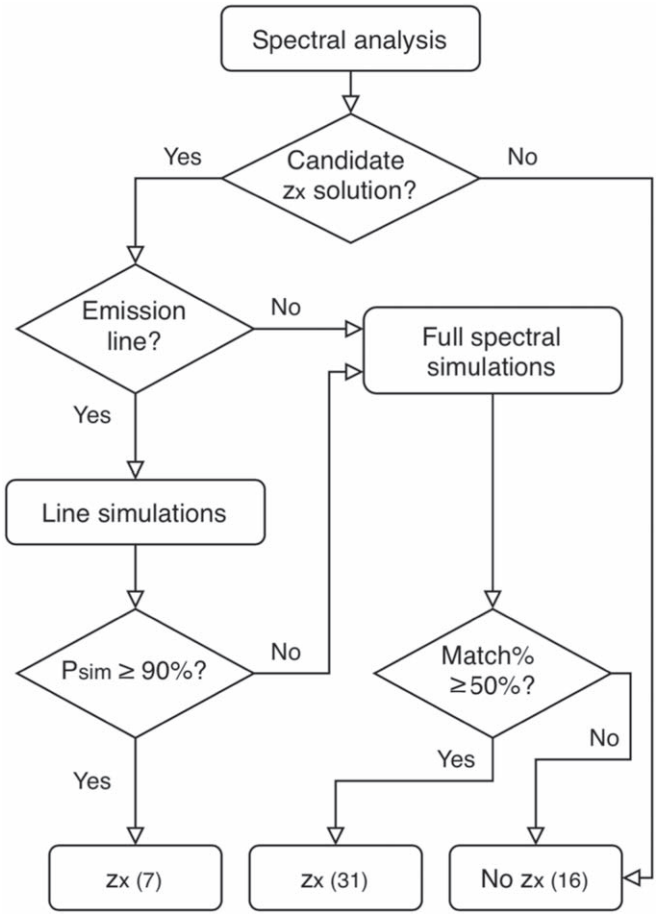

Figure 8. Flowchart of the adopted X-ray procedure. When an X-ray redshift solution was found through the spectral analysis, we first evaluated the significance of possible emission lines (line simulation). If $P_{\rm sim} \geqslant 90\%$, then we got a $z_{\rm X}$ solution from the emission line (seven sources); otherwise, the redshift solution is driven by absorption features. In this case, we checked the redshift reliability through the match percentage (Equation (4), full spectral simulations) with a threshold of $\geqslant$50%, which gave 31 reliable $z_{\rm X}$ solutions. We did not find an X-ray redshift solution for 16 sources.

constant. Here *hyperz* provides primary and secondary $z_{\rm phot}$ solutions, the best-fitting template spectrum, and the reduced χ^2 for each given object. For a detailed description of the code, we refer to Bolzonella et al. (2000). An essential requirement for the SED fitting procedure is an extensive template library that covers the entire range of selected objects without adding unphysical degeneracies. Since the strong ONIR radiation from the accretion disk is heavily extinguished in obscured AGN, allowing the stellar emission of the host galaxy to dominate at these wavelengths (e.g., Merloni et al. 2014), photometric redshifts can be reliably estimated using standard galaxy templates. In this regard, we included the available photometry up to $\sim$5 μm. Above this wavelength, in fact, we expected that the rest-frame emission of the hot dusty torus may overcome the host galaxy stellar emission (e.g., Pozzi et al. 2012; Circosta et al. 2019), invalidating the choice of galaxy templates.

Following Ilbert et al. (2013), we used a library composed of 75 galaxy templates—19 empirical templates derived from the SWIRE library (Polletta et al. 2007), including both elliptical and spiral galaxies (S0, Sa, Sb, Sc, Sd, Sdm), plus 12 starburst templates and 44 additional red galaxy templates generated by Ilbert et al. (2009, 2013) through the Bruzual & Charlot (2003) stellar synthesis models—to better cover the color–redshift space. We built source SEDs using the catalogs described in Table 1; a total of 12 different filters are available from the blue optical to MIR wavelengths. When the same source is revealed in the same filter in more than one catalog, we used the magnitude value from the deepest observation, while if the source is either not detected in a specific band or detected with a signal-to-noise ratio <2, we excluded the corresponding filter from the SED fitting procedure. We searched photometric redshift solutions from $z = 0$ to 7 with a step of $\Delta z = 0.05$. The photometric redshift accuracy also depends on the number of filters in which a specific source is detected. In this regard, S. Marchesi et al. (2021, in preparation) carried out a photometric redshift analysis of all the X-ray sources in the J1030 field, with a similar procedure and data set used in this section. Following this work, we set a threshold of at least five filters that corresponds to an rms $\approx$0.1 when comparing the $z_{\rm phot}$ with the available spectroscopic redshift in the field.

Table 1
Photometric Catalogs Used in Our Analysis

Catalog	Filters	Area	Depth [AB]
MUSYC BVR	*UBVRIz*	$30' \times 30'$	25–26
LBT/LBC	*riz*	$23' \times 25'$	27.5, 25.5, 25.2
CFHT/WIRCam	*YJ*	$24' \times 24'$	23.8, 23.75
MUSYC *K*-wide	*UBVRIzK*	$30' \times 30'$	21
MUSYC *K*-deep	*UBVRIzJHK*	$10' \times 10'$	23
Spitzer/IRAC	ch1 ch2	$35' \times 35'$	22–23

Note. From left: catalog name, filters, covered area, and approximate limiting AB magnitudes.

4.2. Catalogs

In order to correctly reproduce the SED of each individual source, the photometry should sample the same physical region of the host galaxy in all bands. Therefore, the photometric redshift technique uses aperture-corrected magnitudes to account for the flux lost outside the fixed aperture due to the different seeing conditions in different observations. The photometry in the ONIR catalogs (LBT, WIRCam, and MUSYC) was obtained assuming a circular aperture of diameter $\sim$1.″6 (Gawiser et al. 2006; Quadri et al. 2007; Blanc et al. 2008; Morselli et al. 2014; Balmaverde et al. 2017). While in the LBC, WIRCam, and BVR MUSYC catalogs, the aperture correction was already considered, we estimated the aperture-correction terms in the MUSYC *K*-deep and *K*-wide catalogs as follows. For pointlike sources, the difference between total and aperture magnitudes is, by definition, the aperture correction. The $\rm mag_{AUTO}$ entries in the MUSYC *K*-deep and *K*-wide catalogs are a good approximation of the total magnitudes, and in Figure 9, we plotted the difference between them and the aperture magnitudes against the total magnitudes. It is evident that pointlike sources are arranged along a straight line whose value corresponds to the aperture-correction term to be applied to the catalog. We estimated and applied a correction of 0.45 and 0.62 for the MUSYC *K*-deep and *K*-wide catalogs, respectively. All of the ONIR catalogs were then matched together assuming a matching radius of 1″, and the resulting sources were then associated with the X-ray counterparts through a likelihood ratio (Sutherland & Saunders 1992) algorithm,[14] as widely discussed in N20.

[14] https://github.com/alessandropeca/LYR_PythonLikelihoodRatio

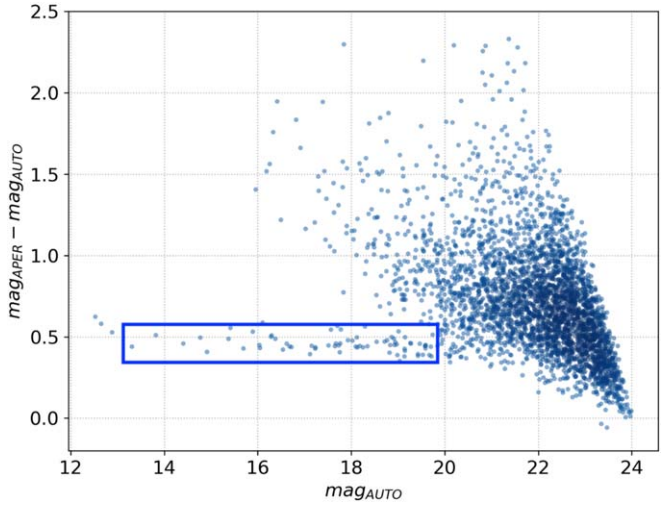

Figure 9. Distribution of the difference between aperture and total *K*-band magnitudes in the MUSYC *K*-deep catalog. The pointlike sources are placed in the blue box, where the mean difference between the two magnitudes corresponds to the seeing aperture-correction term to apply.

The IRAC channels 1 and 2, respectively at 3.6 and 4.5 μm, were introduced to improve the $z_{\rm phot}$ estimate. The inclusion of photometric points at longer wavelengths may increase the best-fit quality, but, due to the low angular resolution of the IRAC camera, separating the emission of close sources was not always possible. Therefore, we performed a visual check to associate the correct MIR counterpart with each X-ray source, and, to avoid any contamination from blended sources, we excluded ambiguous cases from the SED fitting procedure. Unlike the ONIR catalogs, whose aperture extraction diameters are similar, the IRAC fluxes are provided with aperture diameters of 3.″8 and 5.″8. We decided to use the fluxes with the smaller aperture to minimize blending effects. To take into account the larger aperture and different angular resolution, we built the SEDs adding in quadrature $\Delta{\rm mag} = 0.1$ to the IRAC magnitude error of each source in both channel 1 and channel 2.

5. Results

5.1. X-Ray and Photometric Redshift Solutions

The main sample contains 54 X-ray-selected obscured AGN candidates with ≈80 median extracted net counts. Each source has been extensively analyzed in the X-rays and through SED fitting in the ONIR and MIR bands. To verify the goodness and quality of the X-ray redshift solutions, these are now compared with the obtained photometric redshifts. It was possible to estimate an X-ray redshift for 38 (∼70%) sources, down to ∼30 net counts, and a photometric redshift for 46 (∼85%) sources. We do not report X-ray redshift solutions for sources without significant spectral features or when we classified them as unreliable according to the spectral simulations, as discussed in Section 3. Sources without a photometric redshift estimate are those detected in less than five filters. We obtained both $z_{\rm X}$ and $z_{\rm phot}$ solutions for 33 (∼61%) sources, and for all but three there is a redshift estimate from at least one method. For XID 29, 130, and 135, no redshift could be found by any method. The latter two are very faint X-ray sources (only 26 and 39 full-band net counts were extracted, respectively) and lie at very large off-axis angles (10.′0 and 6.′9, respectively). Because of the poor spectral quality, no significant features were detected in their X-ray spectra. Though XID 29 has 133 net counts in the full band and lies at 2.′9, no significant features were found in the X-ray spectrum. While XID 130 is detected only in IRAC, XID 29 and 135 do not reach the threshold on the number of filters, preventing the photometric redshift estimate. All of the obtained redshift solutions are summarized in Table 2, and they represent the first list of redshifts for the J1030 field.

In Figure 10, we show the comparison between the derived X-ray and photometric redshifts. The likelihood profiles of $z_{\rm X}$ and $z_{\rm phot}$ do not always provide a unique solution. In fact, especially for faint sources where the data quality is relatively poor, both distributions may have nonnegligible secondary solutions. If a primary X-ray solution matches (i.e., it is consistent within the errors) with a primary photometric solution (22/33 cases), we discard any secondary solutions. However, the remaining 11 cases (∼20% of the main sample) have secondary solutions, obtained with one method, that match with the primary and unique solutions derived with the other. In these cases, the primary solution from one method can constrain secondary solutions obtained with the other; hence, we selected the agreed redshift as the unique solution (open symbols). There are no cases with a clear match between secondary X-ray and photometric solutions. The blue dots refer to X-ray solutions driven only by absorption features, while the red squares indicate sources in which the 6.4 keV Fe Kα line has been detected. The majority (∼82%) of the solutions are driven by absorption features. As shown in the inset of the same figure, the uncertainties of the X-ray redshift solutions are larger for those sources in which it was not possible to identify any clear Fe Kα emission line. This is explained by the fact that the Fe Kα emission line is a very narrow feature compared to the Fe absorption edge. Thus, in the case of a detected Fe Kα line, the X-ray redshift probability sharply decreases before and after the best-fit value, resulting in a smaller uncertainty.

Overall, there is a good correlation between $z_{\rm X}$ and $z_{\rm phot}$ despite a nonnegligible scatter. Considering a typical accuracy[15] of rms = 0.1 for photometric redshifts obtained with a similar number of filters (e.g., Capak et al. 2004; Zheng et al. 2004; S. Marchesi et al. 2021, in preparation) and rms = 0.1 for the X-ray simulations described in Section 3.2.2, we assumed a confidence region of $\pm 0.15(1+z)$, where 0.15 was computed by summing in quadrature the two rms terms. About 76% of the sources fall within the chosen confidence region (gray dotted lines). We defined as outliers those sources whose $z_{\rm phot}$ value does not lie within the $z_{\rm X}$ 1σ error bars, and the $z_{\rm X}$ value is outside the $0.15(1+z_{\rm phot})$ confidence region. The outlier fraction is then 9% (3/33 sources), and the total fraction of sources where we constrained a redshift solution with both methods is 56% (30/54). We achieved an accuracy of rms = 0.10, and, when considering only the primary solutions with both methods, the rms increases to ≈0.2. These rms values and the outlier fraction are comparable to those obtained in other X-ray redshift techniques. For instance, Simmonds et al. (2018) obtained an rms ≈ 0.2 and 8% outlier fraction when validating against reliable spectroscopic redshifts. This indicates that the assumptions adopted in our procedure can be considered appropriate.

We show one of the sample sources (XID 41) in Figure 11, for which there is a spectroscopic redshift measurement

[15] Defined as rms $= \langle \frac{|z_i - z_j|}{1+z_j} \rangle$, where (z_i, z_j) are $(z_{\rm phot}, z_{\rm spec})$ for photometric redshifts, $(z_{\rm X}, z_{\rm sim})$ for X-ray redshifts, and $(z_{\rm X}, z_{\rm phot})$ in our results.

Table 2
Properties of Obscured AGN Candidates (HR > -0.1 and Net Counts $\geqslant 50$ from N20) in the J1030 Field

XID (1)	Counts Full (2)	HR (3)	$z_{\rm phot}$ (4)	$z_{\rm X}$ (5)	N_H (6)	$F_{\rm X}$ (7)	$L_{\rm X}$ (8)	Feat. (9)
2	890^{+31}_{-30}	$-0.01^{+0.04}_{-0.04}$	$0.70^{+0.02}_{-0.02}$	$0.59^{+0.12}_{-0.36}$	$1.6^{+0.2}_{-0.2}$	$28.39^{+1.25}_{-1.35}$	$8.31^{+0.39}_{-0.39}$	Edge
3	141^{+13}_{-12}	$-0.04^{+0.08}_{-0.08}$	$0.98^{+0.04}_{-0.04}$	-1	$2.4^{+0.8}_{-0.7}$	$5.49^{+0.52}_{-0.53}$	$3.65^{+0.43}_{-0.44}$	⋯
8	115^{+12}_{-11}	$0.07^{+0.11}_{-0.11}$	$3.24^{+0.41}_{-0.04}$	$2.80^{+0.05}_{-0.05}$	$33.4^{+9.9}_{-9.2}$	$3.38^{+0.41}_{-0.46}$	$35.38^{+5.67}_{-5.95}$	Line
11	95^{+11}_{-10}	$0.05^{+0.12}_{-0.12}$	$2.98^{+0.24}_{-0.71}$	$1.94^{+1.05}_{-0.38}$	$27.4^{+8.0}_{-6.9}$	$3.67^{+0.40}_{-0.53}$	$39.41^{+6.11}_{-6.57}$	Edge
15	407^{+21}_{-20}	$0.36^{+0.05}_{-0.05}$	$0.94^{+0.11}_{-0.04}$	-1	$6.4^{+0.6}_{-0.6}$	$13.64^{+0.82}_{-0.84}$	$9.19^{+0.62}_{-0.63}$	⋯
16	55^{+9}_{-8}	$0.03^{+0.16}_{-0.15}$	$1.47^{+0.03}_{-0.05}$	$1.22^{+0.95}_{-0.74}$	$4.4^{+2.5}_{-1.9}$	$1.85^{+0.23}_{-0.34}$	$3.33^{+0.65}_{-0.68}$	Edge
22	65^{+9}_{-8}	$0.05^{+0.16}_{-0.16}$	-1	$2.87^{+0.05}_{-0.06}$	$32.3^{+12.3}_{-9.7}$	$1.51^{+0.31}_{-0.27}$	$17.36^{+3.73}_{-3.79}$	Line
26	261^{+17}_{-16}	$-0.05^{+0.07}_{-0.07}$	-1	$3.47^{+0.16}_{-0.21}$	$23.8^{+6.0}_{-3.8}$	$7.50^{+0.47}_{-0.62}$	$108.52^{+10.28}_{-10.44}$	Edge
28	374^{+20}_{-19}	$-0.07^{+0.06}_{-0.06}$	$1.79^{+0.08}_{-0.08}$	$1.32^{+0.04}_{-0.04}$	<1.6	$8.42^{+0.53}_{-0.64}$	$10.98^{+0.77}_{-0.78}$	Line
29	133^{+17}_{-16}	$0.42^{+0.09}_{-0.09}$	-1	-1	-1	$4.57^{+0.53}_{-0.43}$	-1	⋯
30	200^{+15}_{-14}	$0.32^{+0.08}_{-0.08}$	$0.26^{+0.06}_{-0.02}$	$0.27^{+0.70}_{-0.16}$	$1.9^{+0.3}_{-0.3}$	$5.95^{+0.48}_{-0.50}$	$0.18^{+0.02}_{-0.02}$	Edge
36	204^{+16}_{-15}	$0.38^{+0.08}_{-0.07}$	$0.96^{+0.04}_{-0.02}$	$0.88^{+0.35}_{-0.54}$	$8.1^{+1.2}_{-1.1}$	$9.53^{+0.65}_{-0.87}$	$6.84^{+0.69}_{-0.71}$	Edge
37	79^{+10}_{-9}	$0.18^{+0.14}_{-0.14}$	$1.62^{+0.14}_{-0.08}$	$1.65^{+0.43}_{-1.00}$	$12.3^{+3.4}_{-2.8}$	$2.46^{+0.34}_{-0.37}$	$6.15^{+1.02}_{-1.07}$	Edge
38	119^{+12}_{-11}	$-0.04^{+0.10}_{-0.10}$	$1.16^{+0.05}_{-0.07}$	$1.12^{+1.09}_{-0.68}$	$3.6^{+1.2}_{-1.1}$	$5.79^{+0.76}_{-0.63}$	$5.98^{+0.76}_{-0.78}$	Edge
39	47^{+8}_{-7}	$0.03^{+0.17}_{-0.16}$	$1.47^{+0.09}_{-0.04}$	-1	<5.5	$1.83^{+0.36}_{-0.38}$	$3.18^{+0.69}_{-0.72}$	⋯
40	55^{+9}_{-8}	$0.21^{+0.15}_{-0.15}$	$1.72^{+0.76}_{-0.26}$	-1	$4.8^{+4.1}_{-2.5}$	$2.35^{+0.30}_{-0.40}$	$5.67^{+0.78}_{-1.14}$	⋯
41	118^{+12}_{-11}	$0.02^{+0.11}_{-0.11}$	$2.28^{+0.23}_{-0.32}$	$2.58^{+0.19}_{-0.49}$	$16.8^{+5.1}_{-3.9}$	$3.53^{+0.39}_{-0.45}$	$20.08^{+3.02}_{-2.99}$	Edge
46	121^{+13}_{-11}	$0.06^{+0.10}_{-0.10}$	$2.10^{+0.20}_{-0.09}$	$1.85^{+0.03}_{-0.02}$	$4.4^{+2.3}_{-2.0}$	$5.15^{+0.59}_{-0.64}$	$20.88^{+2.88}_{-2.94}$	Line
47	72^{+10}_{-9}	$0.55^{+0.13}_{-0.13}$	$1.50^{+0.07}_{-0.15}$	$1.38^{+0.32}_{-0.84}$	$16.8^{+4.5}_{-3.6}$	$4.40^{+0.63}_{-0.72}$	$9.79^{+1.80}_{-1.88}$	Edge
48	44^{+9}_{-7}	$0.03^{+0.16}_{-0.16}$	$1.71^{+0.06}_{-0.07}$	-1	<6.8	$1.94^{+0.31}_{-0.32}$	$4.85^{+1.1}_{-1.05}$	⋯
55	52^{+9}_{-7}	$0.02^{+0.15}_{-0.14}$	$0.69^{+0.02}_{-0.04}$	-1	$3.9^{+1.4}_{-1.2}$	$5.86^{+1.08}_{-1.03}$	$1.80^{+0.35}_{-0.38}$	⋯
56	100^{+12}_{-11}	$-0.02^{+0.12}_{-0.11}$	$0.83^{+0.03}_{-0.02}$	-1	$1.7^{+0.8}_{-0.7}$	$3.82^{+0.60}_{-0.41}$	$1.69^{+0.25}_{-0.26}$	⋯
58	28^{+7}_{-6}	$0.43^{+0.20}_{-0.15}$	$2.65^{+0.10}_{-0.06}$	-1	$17.6^{+14.5}_{-6.1}$	$8.34^{+1.93}_{-2.80}$	$61.96^{+21.57}_{-17.4}$	⋯
59	295^{+19}_{-18}	$0.61^{+0.08}_{-0.06}$	$1.00^{+0.03}_{-0.03}$	$0.79^{+0.21}_{-0.38}$	$16.8^{+1.8}_{-1.6}$	$16.63^{+1.02}_{-1.22}$	$15.55^{+1.36}_{-1.37}$	Edge
62	55^{+9}_{-8}	$0.15^{+0.19}_{-0.17}$	-1	$2.76^{+0.11}_{-0.24}$	$47.0^{+-13.4}_{-16.2}$	$4.40^{+0.72}_{-0.92}$	$50.16^{+11.98}_{-12.13}$	Edge
67	205^{+16}_{-15}	$0.16^{+0.08}_{-0.08}$	$0.35^{+0.06}_{-0.10}$	$0.38^{+0.01}_{-0.01}$	$1.3^{+0.3}_{-0.3}$	$6.54^{+0.62}_{-0.62}$	$0.44^{+0.05}_{-0.05}$	Line
69	223^{+17}_{-16}	$0.15^{+0.09}_{-0.09}$	-1	$1.50^{+0.90}_{-0.91}$	$10.5^{+2.0}_{-1.8}$	$8.29^{+0.65}_{-0.69}$	$17.00^{+1.77}_{-1.82}$	Edge
70	215^{+16}_{-15}	$0.28^{+0.07}_{-0.07}$	$0.72^{+0.04}_{-0.03}$	$0.76^{+0.10}_{-0.07}$	$5.1^{+0.7}_{-0.7}$	$10.80^{+0.87}_{-0.76}$	$3.74^{+0.35}_{-0.36}$	Edge
75	109^{+13}_{-12}	$0.60^{+0.14}_{-0.10}$	$0.80^{+0.04}_{-0.01}$	$1.44^{+0.28}_{-0.65}$	$12.1^{+2.5}_{-2.0}$	$10.70^{+1.24}_{-1.64}$	$5.16^{+0.75}_{-0.80}$	Edge
82	123^{+13}_{-12}	$0.24^{+0.13}_{-0.11}$	$4.06^{+0.36}_{-0.45}$	-1	$53.4^{+12.1}_{-11.1}$	$5.29^{+0.76}_{-0.76}$	$154.38^{+22.2}_{-23.74}$	⋯
87	39^{+8}_{-7}	$0.51^{+0.18}_{-0.13}$	$1.56^{+0.10}_{-0.05}$	$1.54^{+0.13}_{-0.07}$	$14.2^{+4.8}_{-3.5}$	$19.23^{+3.63}_{-3.66}$	$14.03^{+3.61}_{-3.64}$	Edge
89	39^{+8}_{-7}	$0.13^{+0.22}_{-0.20}$	$1.01^{+0.05}_{-0.03}$	$1.52^{+0.64}_{-0.92}$	$6.9^{+3.0}_{-2.4}$	$4.28^{+1.06}_{-0.99}$	$3.27^{+0.79}_{-0.89}$	Edge
91	128^{+13}_{-12}	$-0.10^{+0.16}_{-0.17}$	$1.06^{+0.22}_{-0.04}$	$0.92^{+0.03}_{-0.02}$	$1.5^{+0.9}_{-0.8}$	$18.78^{+2.18}_{-2.30}$	$10.41^{+1.37}_{-1.47}$	Line
94	67^{+10}_{-9}	$0.52^{+0.12}_{-0.11}$	$4.08^{+0.10}_{-0.69}$	$2.72^{+0.23}_{-0.14}$	$105.4^{+23.6}_{-20.5}$	$6.50^{+1.08}_{-0.97}$	$155.99^{+26.71}_{-28.57}$	Edge
106	107^{+12}_{-11}	$0.16^{+0.13}_{-0.12}$	$0.53^{+0.02}_{-0.03}$	$0.37^{+0.02}_{-0.02}$	$1.7^{+0.5}_{-0.4}$	$5.09^{+0.52}_{-0.63}$	$0.33^{+0.05}_{-0.05}$	Line
110	120^{+17}_{-16}	$0.22^{+0.17}_{-0.14}$	$0.98^{+0.04}_{-0.08}$	$1.56^{+0.33}_{-0.94}$	$6.4^{+1.8}_{-1.5}$	$6.01^{+0.93}_{-0.91}$	$5.24^{+0.71}_{-0.78}$	Edge
115	40^{+8}_{-7}	$0.52^{+0.14}_{-0.11}$	$0.46^{+0.02}_{-0.03}$	$0.66^{+0.56}_{-0.28}$	$5.2^{+1.9}_{-1.4}$	$5.76^{+1.00}_{-1.31}$	$0.73^{+0.17}_{-0.18}$	Edge
117	33^{+7}_{-6}	$0.04^{+0.20}_{-0.19}$	$3.10^{+0.80}_{-0.60}$	$2.80^{+0.35}_{-1.68}$	$36.0^{+16.3}_{-13.4}$	$4.50^{+1.36}_{-1.00}$	$54.26^{+14.63}_{-15.84}$	Edge
119	46^{+9}_{-7}	$0.30^{+0.17}_{-0.15}$	$0.54^{+0.02}_{-0.02}$	-1	$4.3^{+1.5}_{-1.2}$	$4.31^{+0.76}_{-0.96}$	$0.76^{+0.16}_{-0.17}$	⋯
120	19^{+6}_{-5}	$-0.09^{+0.21}_{-0.21}$	$0.95^{+0.09}_{-0.07}$	-1	<2.1	$4.12^{+1.19}_{-1.59}$	$2.25^{+0.53}_{-0.52}$	⋯
122	82^{+11}_{-10}	$0.29^{+0.13}_{-0.12}$	$1.29^{+0.02}_{-0.04}$	$0.98^{+0.53}_{-0.60}$	$9.6^{+2.9}_{-2.6}$	$6.28^{+0.98}_{-0.85}$	$9.03^{+1.51}_{-1.60}$	Edge
127	35^{+7}_{-6}	$-0.02^{+0.16}_{-0.15}$	$0.05^{+0.03}_{-0.02}$	-1	<1.1	$2.23^{+0.42}_{-0.51}$	$(1.6^{+0.4}_{-0.3})$ e-3	⋯
130	26^{+7}_{-6}	$-0.07^{+0.33}_{-0.32}$	-1	-1	-1	$6.28^{+1.48}_{-1.80}$	-1	⋯
131	39^{+8}_{-7}	$0.05^{+0.23}_{-0.21}$	$1.68^{+0.12}_{-0.15}$	$1.53^{+0.71}_{-0.47}$	$11.8^{+6.2}_{-4.6}$	$4.09^{+0.91}_{-0.94}$	$11.03^{+2.81}_{-3.00}$	Edge
135	34^{+8}_{-6}	$0.05^{+0.20}_{-0.18}$	-1	-1	-1	$3.72^{+0.83}_{-0.76}$	-1	⋯
137	50^{+9}_{-8}	$-0.04^{+0.19}_{-0.18}$	$1.48^{+1.10}_{-0.76}$	-1	<18.7	$4.70^{+0.86}_{-0.87}$	$8.96^{+2.58}_{-3.31}$	⋯
140	40^{+9}_{-7}	$0.02^{+0.24}_{-0.23}$	$0.92^{+0.05}_{-0.04}$	$0.82^{+0.74}_{-0.44}$	<4.0	$2.14^{+0.48}_{-0.45}$	$1.06^{+0.29}_{-0.29}$	Edge
192	138^{+17}_{-15}	1.0	$1.76^{+0.06}_{-0.04}$	$2.20^{+0.15}_{-0.28}$	$77.4^{+15.5}_{-12.5}$	$10.93^{+1.14}_{-1.41}$	$60.94^{+13.66}_{-14.11}$	Edge
196	76^{+10}_{-9}	1.0	$0.54^{+0.02}_{-0.01}$	$0.41^{+0.05}_{-0.25}$	$28.9^{+10.2}_{-5.8}$	$4.67^{+0.43}_{-0.67}$	$1.67^{+0.48}_{-0.37}$	Edge
200	162^{+16}_{-15}	1.0	$1.42^{+0.03}_{-0.04}$	$1.59^{+0.59}_{-0.54}$	$3.4^{+1.4}_{-1.2}$	$6.40^{+0.58}_{-0.75}$	$10.48^{+1.23}_{-1.29}$	Edge
201	55^{+9}_{-8}	1.0	$0.86^{+0.02}_{-0.05}$	$1.15^{+0.08}_{-0.21}$	$34.1^{+10.5}_{-6.9}$	$6.41^{+0.86}_{-1.15}$	$6.12^{+1.63}_{-1.48}$	Edge
207	78^{+11}_{-10}	1.0	$0.14^{+0.03}_{-0.04}$	$0.14^{+0.58}_{-0.09}$	$6.3^{+1.9}_{-1.2}$	$9.50^{+1.43}_{-1.50}$	$0.10^{+0.02}_{-0.02}$	Edge

Table 2
(Continued)

XID (1)	Counts Full (2)	HR (3)	$z_{\rm phot}$ (4)	$z_{\rm X}$ (5)	N_H (6)	$F_{\rm X}$ (7)	$L_{\rm X}$ (8)	Feat. (9)
220	34^{+8}_{-7}	1.0	$1.57^{+0.06}_{-0.08}$	$2.23^{+0.21}_{-0.34}$	$60.5^{+27.9}_{-17.3}$	$6.95^{+1.54}_{-1.41}$	$26.87^{+10.58}_{-10.3}$	Edge
221	30^{+7}_{-6}	1.0	-1	$1.37^{+0.08}_{-0.28}$	$58.8^{+25.1}_{-18.6}$	$8.21^{+1.58}_{-1.95}$	$25.15^{+9.71}_{-9.70}$	Edge

Note. Columns are (1) X-ray ID; (2) net counts in the full (0.5–7 keV) band from the extracted spectra, where the errors were computed according to Gehrels (1986) and correspond to the 1σ level in Gaussian statistics; (3) HR calculated by N20, where we put 1.0 for sources where only hard counts were detected; (4) photometric redshifts obtained from the SED fitting procedure; (5) X-ray redshift solutions; (6) column density in units of 10^{22} cm^{-2}; (7) observed 0.5–7 keV flux in units of 10^{-15} erg s^{-1} cm^{-2}; (8) intrinsic, absorption-corrected luminosity in the 2–10 keV rest-frame band in units of 10^{43} erg s^{-2}; and (9) X-ray feature on which the $z_{\rm X}$ is based, with "line" for the 6.4 keV Fe Kα line and "edge" for the 7.1 keV Fe absorption edge and associated photoelectric cutoff. Here "-1" indicates a nonderived quantity. Uncertainties are reported at the 1σ confidence level.

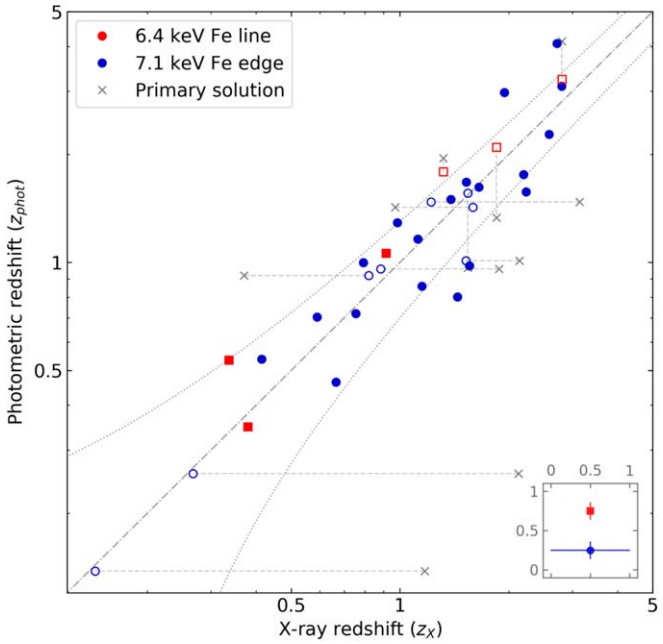

Figure 10. Comparison between X-ray and photometric redshift solutions. The red squares indicate the sources in which the 6.4 keV Fe Kα line was detected, while the blue dots refer to X-ray solutions identified only with absorption features. The open symbols are the secondary solutions constrained by one of the two methods: if a photometric (X-ray) secondary solution is constrained by a single and unique X-ray (photometric) solution, then the shift between the primary photometric (X-ray) solution (gray crosses) and the constrained solution (open symbols) is indicated with a vertical (horizontal) dashed segment. The gray dotted lines indicate the chosen $z_{phot} = \pm 0.15(1 + z_{phot})$ confidence region (see text for details), while the dashed–dotted gray line is the one-to-one relation. In the lower right corner, we show the average 1σ errors for solutions with and without the 6.4 keV Fe Kα line in linear scale and for generic redshifts in both axes.

from Kriek et al. (2008), $z_{spec} = 2.511$. This is the only spectroscopic redshift available so far for our sample. On the one side, we derived an X-ray redshift solution, $z_X = 2.58^{+0.19}_{-0.49}$, by fitting a prominent Fe 7.1 keV edge coupled with the photoelectric absorption cutoff. These features are produced by a heavily obscured yet Compton-thin AGN with $N_H = 1.7^{+0.5}_{-0.4} \times 10^{23}$ cm^{-2} (left panel). On the other side, the derived photometric redshift solution, $z_{phot} = 2.28^{+0.23}_{-0.32}$, is driven by a strong drop in the SED identified at $\sim$12500 Å (right panel). This feature can be associated with a prominent 4000 Å break (e.g., Bruzual 1983; Kauffmann et al. 2003), which indicates that the host is a red and passive galaxy. Both of our solutions are consistent within the uncertainties with the spectroscopic redshift.

5.2. Sample Properties

Given that the good agreement between the two methods validates the obtained redshift solutions, it was possible to conduct a study of the physical and intrinsic X-ray properties of the selected obscured AGN sample. Photometric redshifts generally have smaller uncertainties than the X-ray ones, except for those cases where the Fe Kα line was detected. We therefore decided to use $z_{\rm X}$ when the Fe Kα line was identified and $z_{\rm phot}$ elsewhere. When none of the two above solutions was available, we used absorption-driven $z_{\rm X}$, if estimated. The analysis was then feasible for 51 sources. The redshift distribution (Figure 12, top panel) spans from $\sim$0.1 to $\sim$4 with a median value of $z = 1.3$ and peaks between 0.5 and 1, in agreement with the obscured redshift distributions in other deep X-ray surveys (e.g., Fiore et al. 2008; Georgantopoulos et al. 2008).

We performed the spectral analysis adopting an absorbed power-law model, as described in Section 3.1, but now fixing the redshift. We also carried out a few tests by independently fitting the source and background spectrum using a background model (see Marchesi et al. 2016a for details) and did not find significant differences in the derived best-fit source parameters.

The derived column density distribution (Figure 12, middle panel) ranges between 10^{22} and 10^{24} cm^{-2}, with a mean value of $N_H = 1.7 \times 10^{23}$ cm^{-2} typical of Compton-thin AGN, plus one Compton-thick AGN candidate ($N_H \sim 1.1 \times 10^{24}$ cm^{-2}) at $z \approx 4$. We show the obtained flux distributions in the full, soft, and hard bands in Figure 12 (bottom panel). The derived intrinsic, absorption-corrected, 2–10 keV rest-frame X-ray luminosity is in the range of $\sim 10^{42} - 10^{45}$ erg s^{-1}, with a median value of $L_{2-10\,\rm keV} = 8.3 \times 10^{43}$ erg s^{-1}. We also report a very low ($\sim 10^{40}$ erg s^{-1}) luminosity object (XID 127) whose counterpart is extended in the optical images. It is identified as a very bright nearby galaxy ($z_{phot} = 0.05$, $R = 18$), and its X-ray emission may be produced by a very low luminosity AGN or stellar processes. Overall, we found that the level of obscuration increases as both redshift and luminosity increase (Figure 13). In particular, at $L_{2-10\,\rm keV} < 10^{44}$ erg s^{-1} and $z > 1.5$, AGN with $N_H > 10^{23}$ cm^{-2} start dominating over AGN with column densities between 10^{22} and 10^{23} cm^{-2}. However, we are biased toward the most obscured and luminous objects as the redshift

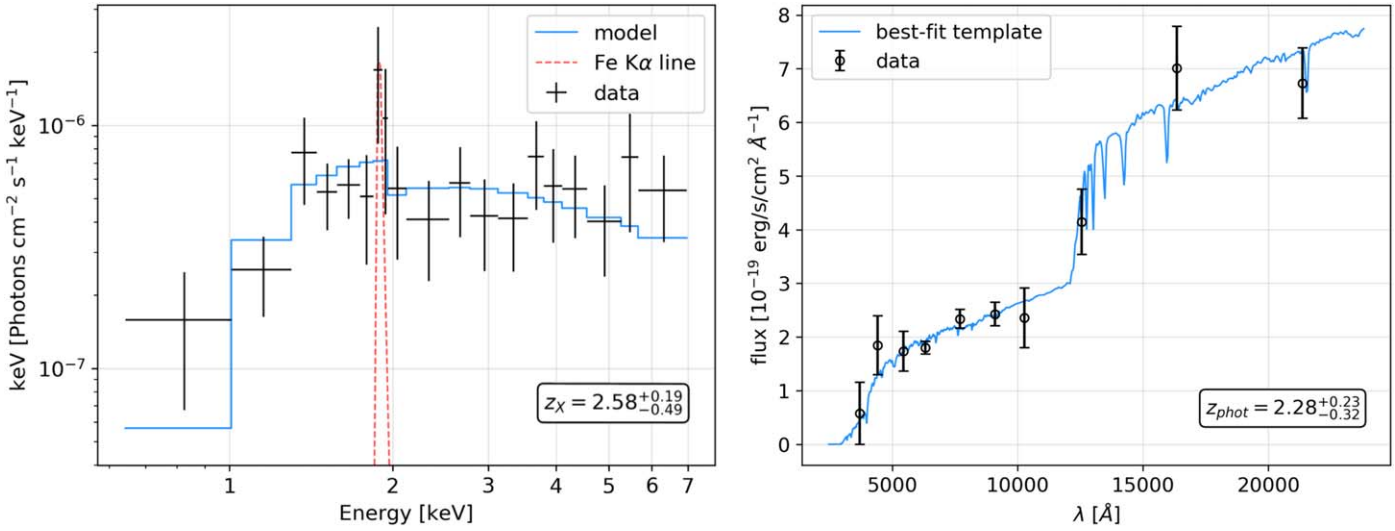

Figure 11. Example of a sample source (XID 41; 118 full-band net counts) with spectroscopic redshift ($z_{spec} = 2.511$; Kriek et al. 2008) in agreement with those obtained by the X-ray spectral analysis and SED fitting. Left panel: X-ray spectrum (black points), rebinned for graphic purposes, with its best-fit model (blue solid line). A prominent Fe 7.1 keV (rest frame) absorption edge at ∼2 keV (observed frame) and a photoelectric absorption cutoff at softer energies are evident. These features are produced by a column density $N_H = 1.7^{+0.5}_{-0.4} \times 10^{23}$ cm^{-2} and drive the X-ray redshift solution. The Fe Kα emission line (red dashed curve) is only tentatively detected (1σ) but not fitted. Right panel: observed SED (black points) and best-fit template (blue solid line), corresponding to a red and passive galaxy where the 4000 Å break is clearly identified at ∼13,000 Å (observed frame).

increases. On the one hand, we lose $N_H < 10^{23}$ cm^{-2} sources at high redshift ($z \gtrsim 3$) because of the HR selection (see Figure 2). In addition, since the X-ray photoelectric absorption cutoff moves toward the lower boundary of the observational band (0.5 keV), the estimate of low N_H values becomes difficult (e.g., Tozzi et al. 2006; Marchesi et al. 2016a). On the other hand, we only see the brightest sources because the sample is flux-limited. We also point out that a fraction of obscured AGN at lower net count regimes (S. Marchesi et. al. 2021, in preparation) is probably missing. Our results are summarized in Table 2.

5.3. Overdensity AGN Candidates

In Gilli et al. (2019), we reported the discovery of a galaxy overdensity at $z \approx 1.7$. The structure has eight members confirmed by secure ONIR spectroscopic redshifts (VLT/MUSE and LBT/LUCI; Gilli et al. 2019), plus three members confirmed by Atacama Large Millimeter/submillimeter Array (ALMA) spectra (D'Amato et al. 2020). Ten of them are star-forming galaxies, and one, located at the center of the overdensity, is a Compton-thick ($N_H = 1.5^{+0.6}_{-0.5} \times 10^{24}$ cm^{-2}) Fanaroff–Riley type II (FRII) radio galaxy. This source is the only one detected in the X-rays (XID 189 in N20). Due to the limited area (∼1′–1.′5) covered around the FRII core by ONIR spectroscopic and ALMA observations, we were able to estimate an overdensity projected size of at least ∼800 kpc. In this work, we found six sources (XID 37, 40, 48, 69, 131, and 137) whose redshift solutions are consistent with $z = 1.7$ and, therefore, may be new overdensity members. In particular, XID 37 and 131 have both photometric and X-ray redshift estimates, while for XID 69 and the remaining sources, we derived only the X-ray and photometric redshift solutions, respectively. Using an angular scale of 8.5 kpc arcsec^{-1}, valid for the adopted cosmology at $z = 1.7$, the projected distances between these sources and the FRII core are in the range 2–4 Mpc, suggesting that the structure may be more extended than previously estimated. The proposed technique can hence be used to identify possible AGN members of cosmological structures, such as galaxy overdensities and protoclusters, which may be extended up to several megaparsecs (e.g., Gilli et al. 2003; Overzier 2016).

6. Discussion

6.1. Reliability of the Obscured AGN Selection from HR Analysis

In Figure 14, we compare the observed HRs as a function of the derived redshifts and column densities with the expected simulated trends. There is a clear distinction between red ($N_H < 10^{23}$ cm^{-2}) and light blue ($10^{23} < N_H < 10^{24}$ cm^{-2}) points. The only candidate at $N_H > 10^{24}$ cm^{-2} (dark blue point) also lies in the corresponding region. This confirms that an HR threshold, carefully calibrated on the data, can be a good proxy for the selection of obscured AGN, as discussed before. However, other than a dependence on the instrument effective area, the expected HR is also a function of the AGN spectral shape, as described in Section 2.3 for typical Γ values.

In the following, we discuss how the HR trends may be influenced by commonly observed AGN spectral features: soft excess and reflection. The soft excess is possibly produced by scattered radiation into the line of sight (e.g., Ueda et al. 2007; Brightman & Nandra 2012) and is emitted over the primary AGN continuum at rest-frame energies below ∼1−2 keV. Especially for high obscuration levels ($N_H > 10^{23}$ cm^{-2}), where the main power-law radiation is strongly extinguished at soft rest-frame energies, the soft excess may give a nonnegligible contribution to the observed soft band, decreasing the HR value for sources up to $z \sim 2-3$. However, its emission is observed to be <10% of the primary component (e.g., Lanzuisi et al. 2015), with typical values of 1%–3% (e.g., Gilli et al. 2007; Ricci et al. 2017), and its contribution to the observed HR is diluted because of the strong decrease of the Chandra collecting efficiency at $E \lesssim 1$ keV. The combination of these factors keeps the HR = −0.1 threshold valid (see

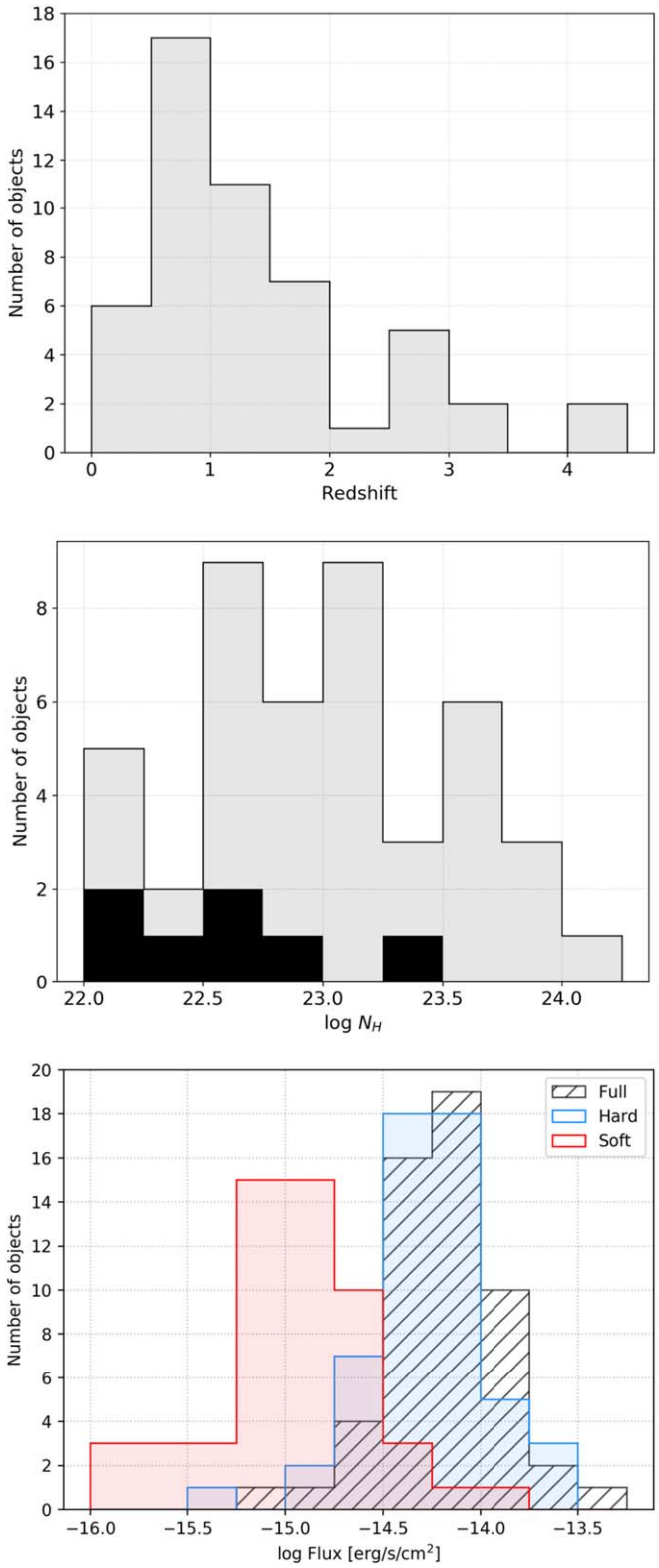

Figure 12. Redshift (top panel) and column density (middle panel) distributions derived from our analysis. Column density upper limits are plotted in black. In the bottom panel, the observed flux distributions in the soft (red), hard (light blue), and full (hatched black) bands are shown.

Appendix B.1). The reflected emission is produced by the reprocessing of the primary X-ray continuum by circumnuclear material, and it may also influence the HR for sources with high

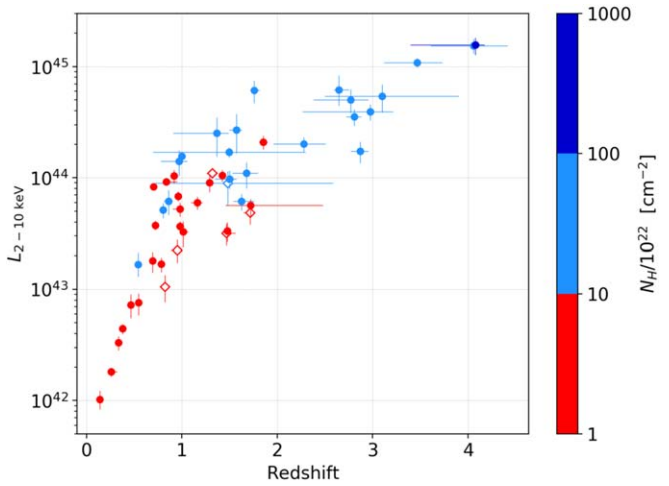

Figure 13. Intrinsic, absorption-corrected luminosity in the 2–10 keV rest-frame band as a function of redshift and N_H in color code. Open diamonds represent N_H upper limits.

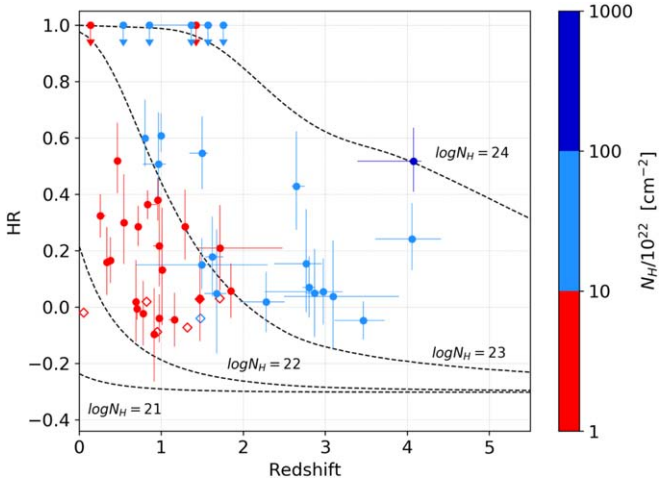

Figure 14. Redshift and column densities (in color code) obtained from our analysis, plotted over the expected HR trends (dashed black lines), computed as discussed in Section 2.3 for $\Gamma = 1.9$ (see also Figure 2). Open diamonds represent N_H upper limits.

N_H. In general, the reflection component peaks at rest-frame energies of ∼30 keV (e.g., Ajello et al. 2008), with a small to moderate contribution in the observed soft band even at a redshift of ∼3−4. As a consequence, we do not expect to miss obscured AGN with the adopted HR selection criteria. A detailed modeling of these spectral components is shown in Appendix B.

6.2. Applicability of the Method

In the following, we discuss the main differences and similarities between our procedure and other X-ray redshift techniques adopted in AGN surveys (e.g., Civano et al. 2005; Iwasawa et al. 2012; Simmonds et al. 2018; Iwasawa et al. 2020).

(i) We constrained X-ray redshifts down to a lower net count regime, ∼30 net counts for particular cases (see Section 3.2.2). This is similar to Simmonds et al. (2018) but markedly different from the hundreds of counts required in other Kα-based redshift derivations. Because the procedure

has strong dependencies on the number of net counts, and considering that it is calibrated on the instrumental response, we expect this net count threshold to be a reliable lower limit for other Chandra deep observations.

(ii) The significance of each X-ray redshift solution is analyzed through extensive simulations based on both local (Section 3.2.1) and, different from any other method, global (Section 3.2.2) backgrounds and responses. For the latter, we directly extracted the background as a function of the off-axis angle to get a realistic background estimate. Then, we rescaled and associated it with the simulated source spectra by taking into account the PSF size and the instrumental response at the source position. Taking into account the off-axis angle effects is crucial to maximize and properly interpret the X-ray information, especially for pointed fields. A different solution for the background handling is to model it. For example, Simmonds et al. (2018) sampled a single representative background for each instrument using archival observations. We refer to that paper for additional information and to Buchner et al. (2014) for details about background modeling in X-ray data.

(iii) As discussed in Section 5.1, there is a nonnegligible fraction (∼20%) of sources in which a secondary redshift solution was constrained by a unique $z_{\rm phot}$ or $z_{\rm X}$. This suggests that the combined use of photometric and X-ray solutions can solve redshift degeneracies that often arise in both methods and may provide better redshift estimates (see, e.g., Vignali et al. 2015; Simmonds et al. 2018; Iwasawa et al. 2020). For this reason, photometric redshifts are included in the procedure, and, for these particular cases, the final redshift solutions are driven by the combination of the two methods.

Considering the above points, the proposed procedure can be used in current X-ray deep fields, where there is still a fraction (∼5%) of X-ray sources without a solid redshift estimate (e.g., Salvato et al. 2009; Marchesi et al. 2016b; Masini et al. 2020). For example, taking sources with at least 50 net counts and HR > -0.1 in the 7 Ms CDF-S (Luo et al. 2017) and AEGIS-XD (Nandra et al. 2015) surveys, the fraction of objects without any redshift estimate is 1%–2% (11 in both fields), and 3%–4% of sources (37 and 26, respectively) are associated only with photometric redshifts that have nonnegligible secondary solutions. Moreover, 11% of sources in the CDF-S are single-line spectroscopic redshifts (e.g., Szokoly et al. 2004), which are often not reliable (e.g., Simmonds et al. 2018; Barger et al. 2019), and the AEGIS-XD survey has 12% of sources marked with a poor quality flag. These cases are optimal for the proposed procedure, which may estimate reliable redshifts from the X-ray spectra alone and/or compare them with the available redshifts to better evaluate secondary photometric solutions and single-line spectroscopic redshift. These sources are potentially high-redshift obscured AGN, which are very challenging to reveal with the current methods (e.g., Cowie et al. 2020) and may contribute to the high-redshift obscured AGN fraction, which is still uncertain and subject to debate (Georgakakis et al. 2017; Vito et al. 2018).

We applied the X-ray redshift procedure to the J1030 field, which lacks the massive spectroscopic coverage of the other X-ray deep fields. Simmonds et al. (2018) showed through simulations that X-ray redshifts may be derived from observations of existing missions (Chandra, XMM-Newton, NuSTAR, Swift/XRT). Similarly, the proposed method can be applied to future deep Chandra and XMM-Newton observations, the forthcoming eRASS surveys (e.g., Merloni et al. 2012), the future Athena observatory (e.g., Aird et al. 2013) and, hopefully, missions under study such as Lynx (e.g., Gaskin et al. 2019) or AXIS (e.g., Mushotzky et al. 2019), which will observe faint, heavily obscured objects with no or extremely faint ONIR counterparts. While eROSITA's soft response and short exposures limit the applicability of X-ray redshift methods (Simmonds et al. 2018), large-area, high-resolution missions such as Athena will likely benefit tremendously from X-ray redshifts. In deep Athena, Lynx, and AXIS surveys, obtaining adequately deep photometric data and/or ONIR spectroscopy will be very costly. Thus, by applying a method similar to the one described in this work and tuning the HR and number of counts thresholds to take into account the effective area of future missions, it will be possible to provide reliable X-ray redshift solutions for obscured AGN.

7. Summary

We proposed a multiwavelength method to constrain the redshifts of X-ray-selected obscured AGN and applied it to the analysis of a sample of 54 candidates in the field around the $z = 6.3$ QSO SDSS J1030+0524. The described technique involves X-ray photometry, spectral analysis, and spectral simulations applied to the Chandra ∼479 ks observational campaign, combined with an SED fitting procedure that includes ONIR and MIR photometry from LBT/LBC (r, i, and z bands), CFHT/WIRCam (Y and J bands), the MUSYC BVR K-wide and K-deep catalogs (U, B, V, R, I, z, J, H, K bands), and Spitzer/IRAC channels 1 and 2 at 3.6 and 4.5 μm, respectively.

Our main results are summarized as follows.

1. We derived reliable X-ray redshifts for a sample of obscured AGN candidates with HR > -0.1. We selected sources in N20 detected with at least 50 full-band net counts so as to identify the main X-ray spectral features, like the Fe Kα 6.4 keV emission line and the Fe 7.1 keV absorption edge. The identified features were then validated through ad hoc spectral simulations.
2. We computed photometric redshifts through an SED fitting procedure to validate the derived X-ray solutions. The comparison between $z_{\rm X}$ and $z_{\rm phot}$ gave an accuracy of rms $= 0.10$ and revealed that the combined use of both methods can constrain secondary solutions from both sides. We obtained a reliable redshift solution with at least one method for 51 (∼94%) sources, with a median value of $z = 1.3$ in the range $z \sim 0.1 - 4$.
3. The obtained redshift solutions were used to derive the X-ray physical intrinsic properties of the sample. We derived a mainly Compton-thin AGN population ($10^{22} \lesssim N_H \lesssim 10^{24}$ cm^{-2}) with a median value of $N_H = 1.7 \times 10^{23}$ cm^{-2} and intrinsic, absorption-corrected, rest-frame 2–10 keV luminosities in the range $10^{42} - 10^{45}$ erg s^{-1} with a median $L_{2-10\,\rm keV} = 8.3 \times 10^{43}$ erg s^{-1}, similar to the distributions observed for obscured AGN in other deep X-ray surveys.
4. We found six possible new AGN members of a galaxy overdensity at $z \approx 1.7$, showing that it may be extended

up to 4 Mpc and that the proposed technique can be used to find candidates of cosmological structures.

5. Finally, we discussed the peculiarities and the feasibility of the proposed method in the context of current X-ray deep surveys, where there is still a fraction of X-ray AGN without a solid redshift estimate, as well as in the context of future X-ray observations with both current and planned X-ray facilities.

We acknowledge the anonymous referee for the useful comments that improved the quality of the paper. A.P. acknowledges D. Costanzo for all the support during the years and Q. D'Amato for the helpful discussions not only about AGN. We acknowledge financial contributions from ASI-INAF No. 2017-14-H.O. N.C. and A.P. kindly acknowledge the NASA-ADAP grant No. 80NSSC18K0418, and the University of Miami.

Appendix A
HR Dependencies

In recent years, the Chandra ACIS camera has experienced a decline in the effective area. Some gaseous material has settled on the cold ACIS optical blocking filters, reducing the photon collection efficiency of the instrument, especially at soft X-ray energies (see the Chandra Proposers' Observatory Guide, December 2019). This has a large impact on the analysis of quantities like the HR, which takes into account both the soft and hard count rates of the observed sources. In this appendix, we analyze the ACIS-I ARF degradation and how this affects the HR analysis. In this regard, we used the aimpoint ARFs available on the dedicated CXC website.[16]

In Figure A1, we show the ratio between the ARFs of different Chandra cycles and that of cycle 10. Below 2 keV, the response is dramatically decreasing with increasing cycles (i.e., years), while at higher energies, the degradation is less significant. As an example, the cycle 20 response at 1 keV is decreased by 80% and 65% compared to cycles 10 and 18, respectively, while at 5 keV, it is decreased by only 4% and <1% compared to the same cycles. In particular, this trend does not allow us to compare our results with the literature (e.g., Tozzi et al. 2001; Szokoly et al. 2004) when the higher photon collection efficiency below 2 keV produced lower HR values for a given spectral shape.

In Figure A2, we compare the differences in HR obtained using the response matrices of cycles 17 (this work) and 10. The difference is lower for the most obscured AGN ($\log N_H = 23, 24$), especially at low redshift. This effect is due to the fact that objects with high N_H have almost only hard X-ray emission, which is collected by the part of the detector less affected by the contaminating material. On the contrary, the difference is larger for sources with low N_H ($\log N_H = 21, 22$) because they also have soft X-ray emission, which is more affected by the detector contamination. Increasing the redshift, part of the rest-frame hard emission is redshifted to lower energies, increasing the differences for sources with high N_H, while this effect is mitigated for sources with low N_H because of the flatter spectral shape.

[16] http://cxc.harvard.edu/caldb/prop_plan/imaging/

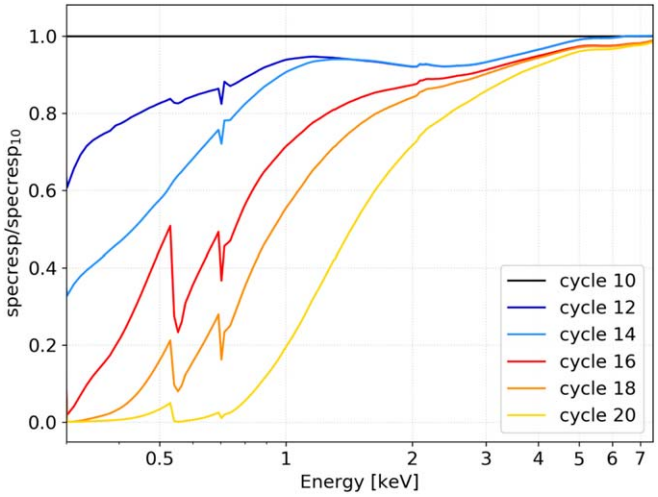

Figure A1. The ACIS-I effective area degradation through the years. We show the ARF ratios between cycles 12 (dark blue), 14 (light blue), 16 (red), 18 (orange), 20 (yellow), and 10 (black).

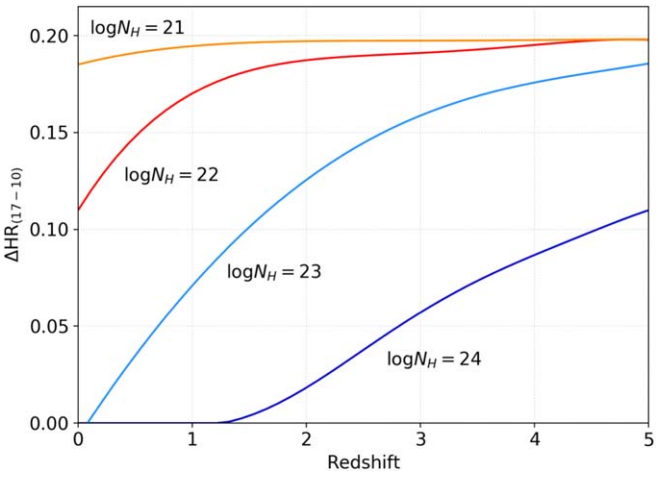

Figure A2. The HR difference between cycles 17 (this work) and 10 as a function of redshift and for different absorption column densities in color code. We assumed a simple absorbed power-law model with a fixed $\Gamma = 1.9$.

Appendix B
Tests for Different Spectral Models

B.1. HR Trends

To validate our HR > -0.1 selection criterion for obscured AGN, we tested how adopting different spectral shapes affects the HR-redshift curves for different N_H values. We recall that the model used in this paper is a simple absorbed power law (hereafter M0; Figure 2). The simulations were performed as discussed in Section 2.3. In each model, the mean Galactic absorption at the J1030 field position ($N_H = 2.6 \times 10^{20}$ cm^{-2}) was considered.

We modeled the soft excess emission, adding a secondary redshifted power law (`zpowerlw`) to M0. The redshift parameter was linked between the components, and no intrinsic absorption was applied to the secondary power law, assuming it is scattered emission into the line of sight. The photon index Γ of the two power laws was fixed to 1.9. The soft excess contribution to the main continuum is observed to be <10%, with typical values of 1%–3% (e.g., Gilli et al. 2007; Ricci et al. 2017), and it was

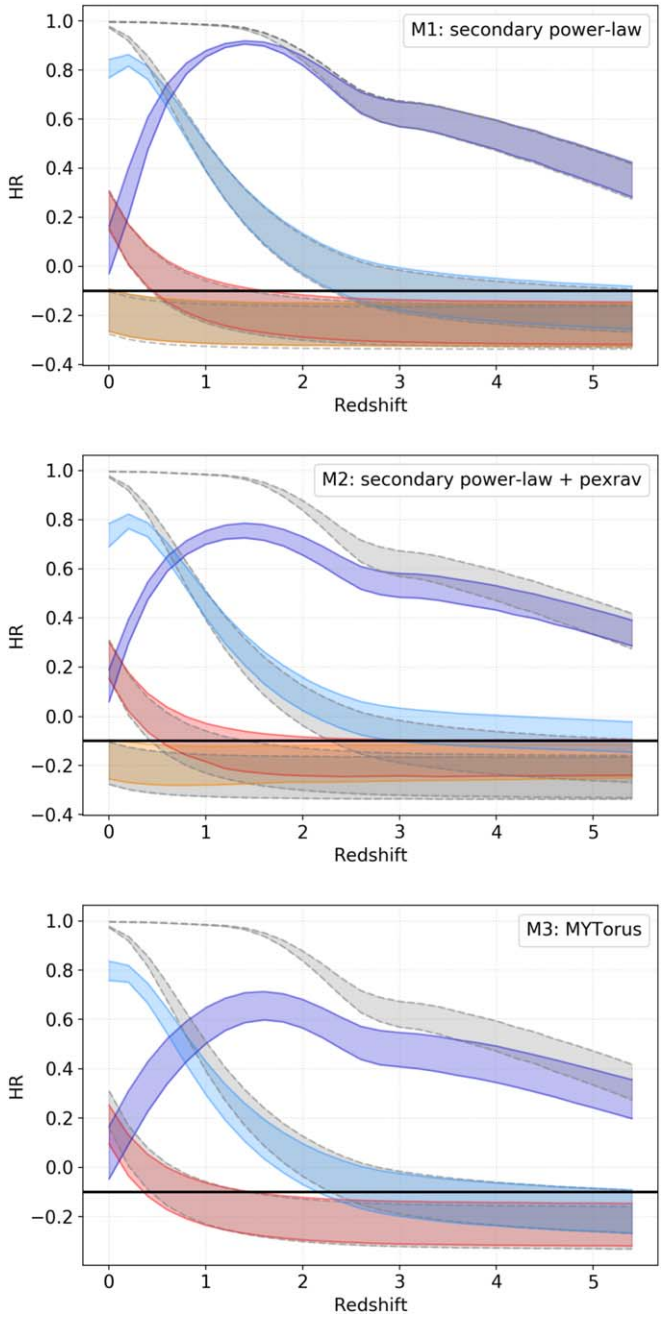

Figure B1. The HR trends as a function of redshift and for different absorption column densities ($\log N_H = 21$, 22, 23, and 24 in orange, red, light blue, and dark blue, respectively). For each N_H, the shaded area represents HR values obtained for different Γ in the range 1.7−2.1. From top to bottom, trends derived with different models are shown: main absorbed power law plus a redshifted secondary power law (M1; top panel), M1 plus a reflection component (M2; middle panel), and the MYTorus model with reflection and a secondary power law (M3; bottom panel). For comparison, the gray shaded areas refer to the single power-law model (M0) used in this paper (see Figure 2). The black solid lines represent the chosen HR = −1 threshold.

considered by adding a multiplicative 3% constant to the secondary power law. The results for this model (hereafter M1) are shown in Figure B1 (top panel). Compared to the M0 curves, there is a strong HR decrease for $\log N_H = 24$ at $z < 2$ (up to $\Delta\mathrm{HR} \sim 0.5$–1 at $z < 0.5$), a small decrease for $\log N_H = 23$ at $z < 0.5$ ($\Delta\mathrm{HR} \sim 0.1$–0.2), and no significant effects for $\log N_H = 22$–21. This is due to the fact that, as the N_H increases, the soft rest-frame main emission is more and more depressed by the absorption, and therefore the soft excess becomes dominant at these energies. This effect is diluted at high redshift, when the primary hard rest-frame emission is redshifted enough to cover the observed-frame soft band.

The reflection is modeled by adding a `pexrav` component (Magdziarz & Zdziarski 1995) to M1. The R value was fixed to −1 (e.g., Marchesi et al. 2016a) to simulate pure reflection, while the photon index and normalization were linked to the main power-law component. The inclination angle and high-energy cutoff were set to the default values $\theta = 60°$ and $E = 100$ keV, respectively. The results for this model (hereafter M2) are shown in Figure B1 (middle panel). There are no major changes in the HR values as a function of redshift compared to the double power-law model. For $\log N_H = 21$, 22, and 23, the HR slightly increases at $z \gtrsim 1$ ($\Delta\mathrm{HR} < 0.1$), while for $\log N_H = 24$, there is an increase at $z < 0.5$ and a decrease at higher redshift ($\Delta\mathrm{HR} \lesssim 0.1$). The `pexrav` model adds flux in both the soft and hard rest-frame bands. Therefore, as a function of redshift and N_H, there is a combination of reflection and soft excess that subtly changes the HR values.

For comparison with M2, in Figure B1 (bottom panel), we show the results obtained with the MYTorus model (Murphy & Yaqoob 2009). It adopts an azimuthally symmetric toroidal shape for the obscuring material, with a fixed half-opening angle of 60°. The torus material is assumed to be neutral, cold, and uniform. The reflection is included within this model but with a more physically motivated treatment, while the soft excess is modeled with a secondary redshifted power law. We refer to this model as M3. We fixed $\Gamma = 1.9$ for all of the components and the inclination angle between the observer and the torus axis to $\theta = 75°$. In MYTorus, $\log N_H$ varies in the range 22–25, so the $\log N_H = 21$ curve is not reported. The curve for $\log N_H = 22$ is very similar to those of M0 and M1. The $\log N_H = 23$ trend is similar to that of M1, and for $\log N_H = 24$, the HR values are lower than those of all other methods (e.g., $\Delta\mathrm{HR} \lesssim 0.1$ compared to M2), with a larger spread for the chosen Γ values. Interestingly, the HR increase at $z \gtrsim 1$ for $\log N_H = 22$ and 23 is not the same as what we observe for M2, due to the different reflection treatment; see also Marchesi et al. (2020) for a comparison between the different shapes of `pexmon` (Nandra et al. 2007), which includes the `pexrav` model, and BORUS (Baloković et al. 2018), a physically self consistent torus model.

In summary, as shown in Figure B1, the HR = −0.1 threshold (black solid line in each panel) remains valid. In fact, with an HR > −0.1, we avoid unobscured sources at any redshift.

B.2. Redshift Match Percentage

We intend to demonstrate here that a simple absorbed power law (M0) is a reasonable model to obtain reliable X-ray redshift estimates. To prove it, we performed several runs of simulations similar to those described in Section 3.2.2 using the M3 model described in Appendix B.1. The explored parameter space is $\log N_H = 22$, 23, and 24 and $z = 0.5$, 1, 2, 3, and 4. We varied the power-law normalization to obtain sources with net counts in the ranges 10–100 (low regime) and 100–1000 (high regime). For each parameter combination, 100 spectra were simulated. The simulated spectra were then fitted with M0 and the three models presented in Appendix B.1: M1 accounts for the soft excess, and M2 and M3 also include the reflection. Compared to M0, treated as in Section 3.2.2, the additional free parameters in M1–M3 were the secondary

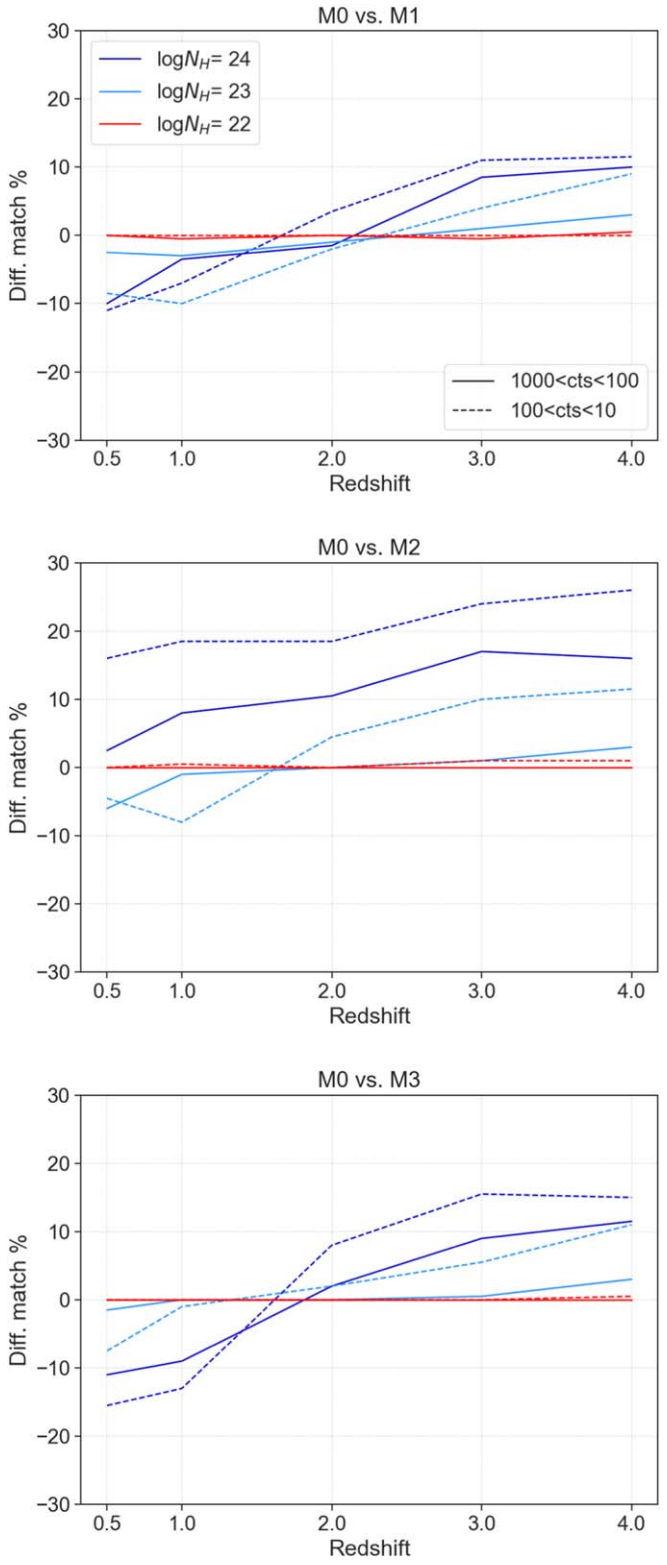

Figure B2. Match percentage difference between M0 and the chosen complex models, M1 (top panel), M2 (middle panel), and M3 (bottom panel), as a function of redshift. Sources with $\log N_H = 22$, 23, and 24 are showed in red, light blue, and dark blue, respectively. The dashed and solid lines represent sources with net count ranges of 10–100 and 100–1000, respectively.

power-law normalization, constrained to be <10% of the primary power law, and the scattering normalization in M3.

In Figure B2, we show the difference in the match percentage (Equation (4)) between the results obtained with M0 and the three complex models. Positive values indicate that M0 is more effective in recovering the simulated source redshift, while negative values indicate that complex models are more efficient. No clear trends are found for $\log N_H = 22$. For $\log N_H = 23$ and 24, there are clear trends as a function of redshift. When compared to M1–M3, M0 is penalized below $z \sim 1$–2, while at higher redshift, it is more effective. This is because the contribution of the secondary power law, present in all of the complex models, influences the fit for sources at low redshift, especially where the primary continuum is strongly extinguished ($\log N_H > 22$) in the soft band. At higher redshift, instead, this contribution is diluted by the redshifted main power law. The reason for these discrepancies is attributed to the increased number of parameters in M1–M3. In particular, the secondary power-law normalization plays an important role, even if constrained to observed values. In fact, the spectral fit may interpret a noise fluctuation as a real spectral shape, fitting a wrong normalization and then a wrong redshift. The more complex the model spectral shape, the higher the risk of misinterpretation. These differences are more evident for higher N_H, as discussed in Appendix B.1, and for the low count regime because of the poor spectral quality.

In general, it is clear that for $\log N_H = 22$, there are no significant differences between the models (<2%), as well as for $\log N_H = 23$ in the high count regime (<5%). For $\log N_H = 24$ and $\log N_H = 23$ in the low count regime, the differences may instead be nonnegligible. For $\log N_H = 23$ in the low count regime, the differences are <10%, while for $\log N_H = 24$, they are <10% and <15% in the high and low count regimes, respectively. Overall, M0 gives better results above $z \sim 1$–2 for all models and is preferable against M2 for $\log N_H = 24$ at any redshift. Below $z \sim 1$–2, M0 is penalized for the remaining cases, with differences within ~10%, except for M3 in the low count regime, $\log N_H = 24$, and $z < 1$, where there is an ~15% difference. However, for M3, there may be a bias introduced by the simulated model, which is the same as the fitted one, that may produce a larger difference in the match percentage against M0.

Given these results, we can safely say that using an absorbed power-law model is a reasonable assumption for the redshift estimate of obscured AGN. The main spectral features, such as the Fe 6.4 keV emission line, the Fe 7.1 keV absorption edge, and the photoelectric absorption cutoff, are included in the absorbed power-law model and are those that drive the redshift solutions. Therefore, for a limited photon statistics, introducing more complex models not only does not substantially improve the results, but it may also introduce degeneracies due to the possible misidentification of complex features.

ORCID iDs

Alessandro Peca https://orcid.org/0000-0003-2196-3298
Cristian Vignali https://orcid.org/0000-0002-8853-9611
Roberto Gilli https://orcid.org/0000-0001-8121-6177
Marco Mignoli https://orcid.org/0000-0002-9087-2835
Riccardo Nanni https://orcid.org/0000-0002-2579-4789
Stefano Marchesi https://orcid.org/0000-0001-5544-0749
Micol Bolzonella https://orcid.org/0000-0003-3278-4607
Marcella Brusa https://orcid.org/0000-0002-5059-6848
Nico Cappelluti https://orcid.org/0000-0002-1697-186X
Andrea Comastri https://orcid.org/0000-0003-3451-9970
Giorgio Lanzuisi https://orcid.org/0000-0001-9094-0984
Fabio Vito https://orcid.org/0000-0003-0680-9305

References

Aird, J., Coil, A. L., Georgakakis, A., et al. 2015, MNRAS, 451, 1892
Aird, J., Comastri, A., Brusa, M., et al. 2013, arXiv:1306.2325
Ajello, M., Rau, A., Greiner, J., et al. 2008, ApJ, 673, 96
Ananna, T. T., Salvato, M., LaMassa, S., et al. 2017, ApJ, 850, 66
Ananna, T. T., Treister, E., Urry, C. M., et al. 2019, ApJ, 871, 240
Antonucci, R. 1993, ARA&A, 31, 473
Arnaud, K. A. 1996, in ASP Conf. Ser., 101, Astronomical Data Analysis Software and Systems V, ed. G. H. Jacoby & J. Barnes (San Francisco, CA: ASP), 17
Balmaverde, B., Gilli, R., Mignoli, M., et al. 2017, A&A, 606, A23
Baloković, M., Brightman, M., Harrison, F. A., et al. 2018, ApJ, 854, 42
Barger, A. J., Cowie, L. L., Bauer, F. E., & González-López, J. 2019, ApJ, 887, 23
Blanc, G. A., Lira, P., Barrientos, L. F., et al. 2008, ApJ, 681, 1099
Bolzonella, M., Miralles, J.-M., & Pelló, R. 2000, A&A, 363, 476
Braito, V., Maccacaro, T., Caccianiga, A., Severgnini, P., & Della Ceca, R. 2005, ApJL, 621, L97
Brandt, W. N., & Alexander, D. M. 2015, A&ARv, 23, 1
Brightman, M., & Nandra, K. 2012, MNRAS, 422, 1166
Brightman, M., Nandra, K., Salvato, M., et al. 2014, MNRAS, 443, 1999
Broos, P. S., Townsley, L. K., Feigelson, E. D., et al. 2010, ApJ, 714, 1582
Brusa, M., Zamorani, G., Comastri, A., et al. 2007, ApJS, 172, 353
Bruzual A, G. 1983, ApJ, 273, 105
Bruzual, G., & Charlot, S. 2003, MNRAS, 344, 1000
Buchner, J., Georgakakis, A., Nandra, K., et al. 2014, A&A, 564, A125
Buchner, J., Georgakakis, A., Nandra, K., et al. 2015, ApJ, 802, 89
Calzetti, D., Armus, L., Bohlin, R. C., et al. 2000, ApJ, 533, 682
Capak, P., Cowie, L. L., Hu, E. M., et al. 2004, AJ, 127, 180
Cash, W. 1979, ApJ, 228, 939
Ciliegi, P., Zamorani, G., Hasinger, G., et al. 2003, A&A, 398, 901
Circosta, C., Vignali, C., Gilli, R., et al. 2019, A&A, 623, A172
Civano, F., Comastri, A., & Brusa, M. 2005, MNRAS, 358, 693
Civano, F., Elvis, M., Brusa, M., et al. 2012, ApJS, 201, 30
Comastri, A., Setti, G., Zamorani, G., & Hasinger, G. 1995, A&A, 296, 1
Cowie, L. L., Barger, A. J., Bauer, F. E., & González-López, J. 2020, ApJ, 891, 69
D'Amato, Q., Gilli, R., Prandoni, I., et al. 2020, A&A, 641, L6
Elvis, M., Hao, H., Civano, F., et al. 2012, ApJ, 759, 6
Fabian, A. C., Iwasawa, K., Reynolds, C. S., & Young, A. J. 2000, PASP, 112, 1145
Fiore, F., Grazian, A., Santini, P., et al. 2008, ApJ, 672, 94
Freeman, P. E., Kashyap, V., Rosner, R., & Lamb, D. Q. 2002, ApJS, 138, 185
Gaskin, J. A., Swartz, D. A., Vikhlinin, A., et al. 2019, JATIS, 5, 021001
Gawiser, E., van Dokkum, P. G., Herrera, D., et al. 2006, ApJS, 162, 1
Gehrels, N. 1986, ApJ, 303, 336
Georgakakis, A., Salvato, M., Liu, Z., et al. 2017, MNRAS, 469, 3232
Georgantopoulos, I., Georgakakis, A., Rowan-Robinson, M., & Rovilos, E. 2008, A&A, 484, 671
Ghisellini, G., Haardt, F., & Matt, G. 1994, MNRAS, 267, 743
Giacconi, R., Rosati, P., Tozzi, P., et al. 2001, ApJ, 551, 624
Gilli, R., Cimatti, A., Daddi, E., et al. 2003, ApJ, 592, 721
Gilli, R., Comastri, A., & Hasinger, G. 2007, A&A, 463, 79
Gilli, R., Mignoli, M., Peca, A., et al. 2019, A&A, 632, A26
Hickox, R. C., & Alexander, D. M. 2018, ARA&A, 56, 625
Hsu, L.-T., Salvato, M., Nandra, K., et al. 2014, ApJ, 796, 60
Ikeda, S., Awaki, H., & Terashima, Y. 2009, ApJ, 692, 608
Ilbert, O., Capak, P., Salvato, M., et al. 2009, ApJ, 690, 1236
Ilbert, O., McCracken, H. J., Le Fèvre, O., et al. 2013, A&A, 556, A55
Iwasawa, K., Comastri, A., Vignali, C., et al. 2020, A&A, 639, A51
Iwasawa, K., Gilli, R., Vignali, C., et al. 2012, A&A, 546, A84
Kalberla, P. M. W., Burton, W. B., Hartmann, D., et al. 2005, A&A, 440, 775
Kauffmann, G., Heckman, T. M., Tremonti, C., et al. 2003, MNRAS, 346, 1055
Kriek, M., van Dokkum, P. G., Franx, M., et al. 2008, ApJ, 677, 219
Lanzuisi, G., Civano, F., Elvis, M., et al. 2013a, MNRAS, 431, 978
Lanzuisi, G., Civano, F., Marchesi, S., et al. 2013b, ApJ, 778, 62
Lanzuisi, G., Ranalli, P., Georgantopoulos, I., et al. 2015, A&A, 573, A137
Luo, B., Brandt, W. N., Xue, Y. Q., et al. 2010, ApJS, 187, 560
Luo, B., Brandt, W. N., Xue, Y. Q., et al. 2017, ApJS, 228, 2
Maccacaro, T., Braito, V., Della Ceca, R., Severgnini, P., & Caccianiga, A. 2004, ApJL, 617, L33
Magdziarz, P., & Zdziarski, A. A. 1995, MNRAS, 273, 837
Mainieri, V., Bergeron, J., Hasinger, G., et al. 2002, A&A, 393, 425
Marchesi, S., Civano, F., Elvis, M., et al. 2016b, ApJ, 817, 34
Marchesi, S., Gilli, R., Lanzuisi, G., et al. 2020, A&A, 642, A184
Marchesi, S., Lanzuisi, G., Civano, F., et al. 2016a, ApJ, 830, 100
Masini, A., Hickox, R. C., Carroll, C. M., et al. 2020, ApJS, 251, 2
Merloni, A., Bongiorno, A., Brusa, M., et al. 2014, MNRAS, 437, 3550
Merloni, A., Predehl, P., Becker, W., et al. 2012, arXiv:1209.3114
Morselli, L., Mignoli, M., Gilli, R., et al. 2014, A&A, 568, A1
Murphy, K. D., & Yaqoob, T. 2009, MNRAS, 397, 1549
Mushotzky, R., Aird, J., Barger, A. J., et al. 2019, BAAS, 51, 107
Nandra, K., Laird, E. S., Aird, J. A., et al. 2015, ApJS, 220, 10
Nandra, K., O'Neill, P. M., George, I. M., & Reeves, J. N. 2007, MNRAS, 382, 194
Nandra, K., & Pounds, K. A. 1994, MNRAS, 268, 405
Nanni, R., Gilli, R., Vignali, C., et al. 2018, A&A, 614, A121
Nanni, R., Gilli, R., Vignali, C., et al. 2020, A&A, 637, A52
Oke, J. B. 1974, ApJS, 27, 21
Overzier, R. A. 2016, A&ARv, 24, 14
Padovani, P., Alexander, D. M., Assef, R. J., et al. 2017, A&ARv, 25, 2
Piconcelli, E., Jimenez-Bailón, E., Guainazzi, M., et al. 2005, A&A, 432, 15
Planck Collaboration, Ade, P. A. R., Aghanim, N., et al. 2016, A&A, 594, A13
Polletta, M., Tajer, M., Maraschi, L., et al. 2007, ApJ, 663, 81
Pozzi, F., Vignali, C., Gruppioni, C., et al. 2012, MNRAS, 423, 1909
Protassov, R., van Dyk, D. A., Connors, A., Kashyap, V. L., & Siemiginowska, A. 2002, ApJ, 571, 545
Quadri, R., Marchesini, D., van Dokkum, P., et al. 2007, AJ, 134, 1103
Ricci, C., Trakhtenbrot, B., Koss, M. J., et al. 2017, ApJS, 233, 17
Risaliti, G., & Elvis, M. 2004, in Supermassive Black Holes in the Distant Universe, Astrophysics and Space Science Library, ed. A. J. Barger, Vol. 308 (Dordrecht: Kluwer), 187
Salvato, M., Hasinger, G., Ilbert, O., et al. 2009, ApJ, 690, 1250
Salvato, M., Ilbert, O., & Hoyle, B. 2019, NatAs, 3, 212
Simmonds, C., Buchner, J., Salvato, M., Hsu, L. T., & Bauer, F. E. 2018, A&A, 618, A66
Sutherland, W., & Saunders, W. 1992, MNRAS, 259, 413
Szokoly, G. P., Bergeron, J., Hasinger, G., et al. 2004, ApJS, 155, 271
Tozzi, P., Gilli, R., Mainieri, V., et al. 2006, A&A, 451, 457
Tozzi, P., Rosati, P., Nonino, M., et al. 2001, ApJ, 562, 42
Treister, E., & Urry, C. M. 2006, ApJL, 652, L79
Ueda, Y., Akiyama, M., Ohta, K., & Miyaji, T. 2003, ApJ, 598, 886
Ueda, Y., Eguchi, S., Terashima, Y., et al. 2007, ApJL, 664, L79
Urry, C. M., & Padovani, P. 1995, PASP, 107, 803
Vignali, C., Iwasawa, K., Comastri, A., et al. 2015, A&A, 583, A141
Vito, F., Brandt, W. N., Yang, G., et al. 2018, MNRAS, 473, 2378
Wachter, K., Leach, R., & Kellogg, E. 1979, ApJ, 230, 274
Yu, H., Tozzi, P., Borgani, S., Rosati, P., & Zhu, Z. H. 2011, A&A, 529, A65
Zheng, W., Mikles, V. J., Mainieri, V., et al. 2004, ApJS, 155, 73